EXPERIMENTALLY VALIDATED NEUTRON FLUX SIMULATION FOR TRIGA LARGE IRRADIATION CELL

A Thesis

by

JAMES BRANDON TOMPKINS

Submitted to the Office of Graduate and Professional Studies of
Texas A&M University
in partial fulfillment of the requirements for the degree of

MASTER OF SCIENCE

Chair of Committee,	Ryan G. McClarren
Committee Members,	Bani Mallick
	Jean C. Ragusa
Head of Department,	Yassin A. Hassan

August 2016

Major Subject: Nuclear Engineering

ABSTRACT

The one megawatt TRIGA reactor at Texas A&M has various methods of irradiating samples, but one of the most unique dose positions is severely underutilized. This irradiation cell is a large space where samples may be placed for activation by moving the reactor bridge to a window on the wall of the cell and operating the reactor. Due to the cell's large size, neutron flux for experiments is difficult to resolve spatially, giving predictions of dose to samples a high level of uncertainty. To this end, Parallel Deterministic Transport (PDT), a rapidly maturing radiation transport code, is used to simulate the neutron flux distribution for reactor experiments in the cell. By utilizing PDT, a model for the cell is created, and experiments are performed to validate the computational results benefitting both the Nuclear Science Center (NSC) and PDT development. To construct the PDT model, the cell's geometry, material properties, and boundary conditions are necessary. By measuring the cell, identifying construction materials, and performing experiments to measure flux at various cell locations, input to the computational model is developed by constructing a mesh reflecting cell geometry, processing neutron interaction cross sections for cell materials, and fitting a surface to flux collected on the boundary, then discretizing flux in angle. After the model is constructed, it is validated by perturbing the boundary condition using error from the surface fit in an attempt to generate model results that bound the experimental data. While the model results in the epithermal region would benefit from inclusion of higher energy groups, the thermal model results bound almost half of the experiment data, giving confidence in the method's increased accuracy in future work.

ACKNOWLEDGEMENTS

Thanks go out to NSC directors Drs. Radek Skoda and Sean McDeavitt for greenlighting and approving resources for data collection. Additionally, NSC research engineer Jan Vermaak provided his MCNP NSCR core model used in calibrating model angular discretization. Further gratitude is given to NSC student operations staff as many aided in data collection by setting up dry cell experiments and counting flux foils. Several PDT staff and students have been essential to setting up code inputs and model properties. Much thanks to Daryl Hawkins for aiding in creation of PDT inputs and compiling PDT on LLNL's cab machine as well as obtaining computing accounts for external systems at LLNL through the SARAPE program. Blaise Barney at the Livermore Computing Center deserves recognition for his speedy email responses and outstanding patience with a new HPC user, and sincerest gratitude is offered to Livermore Computing for allowing students to use their supercomputing facilities. Faculty members in the Nuclear Engineering department at Texas A&M have been integral not only for guiding this research, but for spearheading the development of tools to allow this study to take place. Drs. Marvin Adams and Jean Ragusa have provided valuable input for the project, and Dr. Jim Morel furnished various resources through the Center for Large-Scale Scientific Simulations. The chair of this committee Dr. Ryan McClarren has contributed limitless guidance and valuable recommendations throughout this study. Lastly, Assistant Director of the NSC Jerry Newhouse not only got this project off the ground, but was largely responsible for identifying the need for a model of the dry cell and shaping the project's direction as it grew. He is thanked as a contributor and friend.

NOMENCLATURE

CLASS	Center for Large-Scale Scientific Simulations
DOE	Department of Energy
HPGe	High Purity Germanium Counter
LC	Livermore Computing
LDFE	Linear Discontinuous Finite Element
LLNL	Lawrence Livermore National Laboratory
MCNP	Monte Carlo N-Particle Code
NEAMS	Nuclear Energy Advanced Modeling and Simulation
NSC	Nuclear Science Center
NSCR	Nuclear Science Center Reactor
OECD	Organisation for Economic Co-operation and Development
ORNL	Oak Ridge National Laboratory
PDT	Parallel Deterministic Transport Code
TAMU	Texas A&M University
TEES	Texas Engineering Experiment Station
TRIGA	Training Research Isotope Production General Atomics Reactor
UQ	Uncertainty Quantification
V&V	Verification and Validation

TABLE OF CONTENTS

Page

LIST OF FIGURES

FIGURE Page

LIST OF TABLES

TABLE Page

1. INTRODUCTION

The Nuclear Science Center at Texas A&M University is one of the oldest facilities with an operational research reactor having first opened in December 1961 with continued safe and efficient operation to this day [2]. The recently renewed operation license from the Nuclear Regulatory Commission ensures that this facility will remain steadfast in its mission to advance nuclear research for at least the next twenty years, but to maintain competitive experimental capability as an irradiation facility, the NSC must be able to accurately predict sample dose and ensure these predictions consistently agree with experimental results. Locations frequently utilized for sample irradiation are small enough that a single, volume averaged neutron flux value is sufficient to predict sample dose which can be easily measured to inform dose predictions. Yet, some of the NSC's experimental facilities have fallen into obsolescence due to the flux being spatially distributed throughout the irradiation location's volume requiring more exhaustive studies to accurately characterize sample dose.

One such experimental location unique to the NSC is the large irradiation cell. This is an open space that accommodates samples of various size to be irradiated by either the NSC TRIGA reactor or a lanthanum source charged by the reactor depending upon desired dose for the experiment. By being one of the few nuclear research centers with facilities large enough to accomodate industrial scale equipment in a heavily irradiated environment, the NSC currently stands to benefit from the the foresight of its original designers with the availability of the irradiation cell's capabilities. With an eye to increase experimental capacity to contemporary testing applications (e.g. electronic radiation hardening and material radiation resistance)

for a broad range of sample types and sizes, the NSC has begun to consider the irradiation cell a potentially lucrative resource.

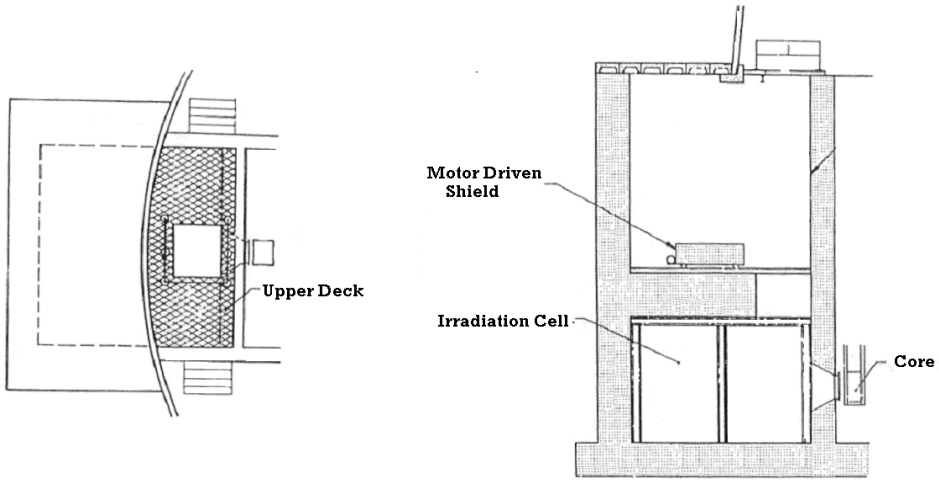

Figure 1.1: Top and side (facing north) views of large irradiation cell [2].

The large irradiation cell is an open space with an area of about eighteen feet by sixteen feet at the same elevation of the NSC TRIGA's pool floor. Samples irradiated in the cell can range from as small as a flux foil (less than one cubic centimeter in volume) to industrial scale samples (several cubic meters), and either the NSC TRIGA or a lanthanum source can be employed as the experiment source. The cell is generally used for gamma irradiations where large uncertainties in dose are acceptible due to little information being available for the neutron dose in the cell during reactor operations. An aluminum window separates the cell from the pool where the TRIGA operates. The reactor's west face may be fixed within a few inches of this window on the pool side to irradiate samples in the cell as illustrated by Figure 1.1. Concrete walls several feet thick to the sides of the window effectively make the window the only significant source of radiation into the cell. With a source

of radiation being incident upon the cell at and around only the window, the neutron flux will have high angular dependence making Boltzmann transport an ideal method to characterize the neutron flux in the cell. Steel structural beams support the cell, but often become activated enough in the course of reactor driven experiments to delay sample extraction as the beams need to decay. A table with a lead box to shield samples from less penetrative radiation is also present in the cell and able to be moved toward or away from the the window with a rail system on the floor.

The cell already has large experimental potential, but lack of predictive capabilities for experiment dose seems to be the main barrier to overcome the cell's current disuse. Due to the cell's large size, neutron flux for experiments is difficult to resolve spatially giving predictions of dose to samples a high level of uncertainty, making potential researchers unwilling to trust the cell as a viable irradiation position for expensive materials or equipment tests. If the neutron flux in the cell can be characterized spatially, not only will the NSC gain a useful sample dose prediction method but increase its research potential.

To engender the confidence of potential researchers, emissions within the cell must first be identified and characterized. When operating the reactor in the configuration shown in Figure 1.1, various forms of radiation permeate the large cells environment, but researchers are often only interested in the dose from neutrons and/or gamma particles. In the interest of maximizing the research cabability impact of this work, low energy neutrons are investigated due to their higher interaction cross sections in cell materials and effectiveness at approximating accelerated radiation damage. Low energy neutrons are fairly easy to measure when using a technique such as neutron activation analysis (NAA), but in a space so large, it would take a monumental effort to map the flux of the entire cell [19]. However, by utilizing the ease of taking flux measurements in a small area from NAA to inform a radiation transport simulation,

not only would a comprehensive characterization of neutron flux within the cell be provided, but by perturbing the inputs to these simulations, a measure of validation can be achieved for the compuational results at experimental positions in the cell.

The cell is physically measured to construct a mesh that approximates its geometry. A simple tape measure, pen, and paper are all that is needed to quantify the cell spatially then material bounds recorded in a spreadsheet. In order to provide material properties and neutron interaction cross sections to the transport simulation, cell materials must be identified. After establishing materials within the cell, their material properties and elemental composition need to be found to provide to the simulation and process cross sections. With the geometry and material properties recorded, only the boundary condition is needed to create the cell's computational model. To develop the boundary condition, experiments are conducted to quantify flux at various positions throughout the cell using gold-aluminum flux foils. The foils are counted on a high purity germanium detector and the counts used to calculate flux at the foils' experimental positions. The flux points measured on the cell window are fit to a surface and flux at vertices of the discretized geometry extracted to use as flux boundary magnitudes in the computational model. The fitted fluxes are discretized in angle then able to be used as the boundary condition input.

From a predictive science standpoint, challenges in characterizing neutron dose in the irradiation cell include the size of the problem and numerous predictors for the quantity of interest. The cell measures approximately 484 cm long, 548 cm wide and 292 cm tall, but samples on the order of a few cubic centimers are not uncommon in experiments in this location. How finely the simulation's mesh is divided will largely determine the efficacy of the models flux predictions spatially thus more accurately able to provide sample dose, but higher spatial resolution also increases the degrees of freedom within the problem making the simulation more computationally tax-

ing. Neutron flux will vary based on numerous parameters for this setup including positioning of the reactor, incident flux magnitude, and operational considerations (e.g. buildup of fission products such as xenon requiring higher reactivity insertion to attain a specific power). Some of these may be mitigated by consistency in experimentation such as only taking data from the first start up of the reactor every week to limit fission product buildup or ensuring the reactor bridge is locked in the same position for each experiment, but epistemic uncertainty in experiment results are witnessed by the variation of incident flux measurements under nearly identical operational conditions necessitating statistical analysis.

To bridge the gap between the two mindsets of experiment results as fact and modeling results as circumspect, it is vital to demonstrate the validity of advanced solution techniques using validation data from experiments. Uncertainty quantification (UQ), verification, and validation (V&V) have become so widely recognized in the nuclear industry as imperative areas of development that the Office of Nuclear Energy's Advanced Modeling and Simulation (NEAMS) team has named them specifically as research initiatives [16]. As more advanced simulation tools become available, validation methods will be integral in demonstrating a tool's utility to researchers and ensure that simulations accurately reflect solutions to engineering problems. Validating PDT for the irradiation cell problem using data collected from cell experiments establishes a validation methodology for discrete ordinates transport simulations. By using this code as it is actively under development to model an experimental location, confidence in PDT's predictive capabilities can grow with promising results and if results from the simulation are shown to be accurate, the findings may revitalize a largely underused unique experimental facility at the NSC.

2. RESEARCH FOUNDATIONS

To establish the background of this work, an investigation of contemporary research in the field is in order. The theory, equipment, and computational resources utilized are first described then placed in context of the work by illustrating the method's applicability and how it interacts with other components of the research foundations. By explaining how each applies to the work performed as well as how concepts work together, a better understanding of the research methodology is reached.

2.1 Theory and Methods

The fundamentals of any study both justify the investigation and place it in context with contemporary work. By demonstrating that methods used as the basis for this work are commonly employed throughout the field of study, the robustness of methods, and their applicability to the work, a measure of confidence in utilizing these practices for the problem at hand is achieved. As neutron flux characterization is of principal interest to this study, modern methods of radiation transport and material property conditioning are examined. Processing of continuous neutron interaction cross sections of isotopes into group averaged material cross sections serviceable for radiation transport simulations is another topic covered, and the physics supporting the technique for measuring neutron dose are detailed.

2.1.1 Neutron Transport

As one of the main objectives of this study is to develop a model for the distribution of neutron flux within the irradiation cell, a way of characterizing the behavior of these particles within a system is necessary. Generally, some form of radiation

transport is employed for this task as describing the interactions each group of particles may undergo in a conservation statement has both been extensively investigated as a viable approach and only requires a spatial system that describes the problem, material distribution within the problem's geometry, and the conditions on the system's boundaries to obtain a solution [8].

The Boltzmann transport equation,

$$\frac{1}{v(E)}\frac{\partial\Phi}{\partial t} + \hat{\Omega}\cdot\nabla\Phi + \Sigma_t\Phi = \frac{\chi_p(E)}{4\pi}\int_0^\infty dE'\nu_p(E')\Sigma_f(\vec{r},E',t)\phi(\vec{r},E',t)+$$
$$\int_{4\pi} d\hat{\Omega}'\int_0^\infty dE'\Sigma_s(\vec{r},E')f'(\vec{r},\hat{\Omega}'\rightarrow\hat{\Omega},E'\rightarrow E,t)\Phi(\vec{r},\hat{\Omega}',E',t)+\sum_{i=1}^{N}\frac{\chi_{di}(E)}{4\pi}\lambda_i C_i(\vec{r},t) \tag{2.1}$$

is a deterministic conservation statement of neutron behavior [8]. Each term in this integro-differential equation identifies a type of interaction that neutrons in this system experience, with sinks and losses on the left side of the Eq. 2.1 and sources on the right [8].

Table 2.1: Transport Equation Terms and Interactions Represented [8].

Mathematical Representation	Physical Interpretation
$\frac{1}{v(E)}\frac{\partial\Phi}{\partial t}$	transient (time dependent) term
$\hat{\Omega}\cdot\nabla\Phi$	streaming term
$\Sigma_t\Phi$	total neutron interaction density
$\frac{\chi_p(E)}{4\pi}\int_0^\infty dE'\nu_p(E')\Sigma_f(\vec{r},E',t)\phi(\vec{r},E',t)$	fission rate density for group
$\int_{4\pi} d\hat{\Omega}'\int_0^\infty dE'\Sigma_s(\vec{r},E')$ $f'(\vec{r},\hat{\Omega}'\rightarrow\hat{\Omega},E'\rightarrow E,t)\Phi(\vec{r},\hat{\Omega}',E',t)$	group scattering density
$\sum_{i=1}^{N}\frac{\chi_{di}(E)}{4\pi}\lambda_i C_i(\vec{r},t)$	fission product delayed neutron contribution

Several of these terms may be simplified or eliminated altogether depending upon the system of interest. In the case of the irradiation cell, the time dependent term is unnecessary as only the steady state scalar flux at specific reactor thermal power levels is of interest, and because none of the material within the cell is fissile or fissionable, both the fission and delayed neutron source terms may be omitted. The reduced transport equation applying to the large irradiation cell is then

$$\hat{\Omega} \cdot \nabla \Phi + \Sigma_t \Phi = \int_{4\pi} d\hat{\Omega}' \int_0^{\infty} dE' \Sigma_s(\vec{r}, E') f'(\vec{r}, \hat{\Omega}' \rightarrow \hat{\Omega}, E' \rightarrow E) \Phi(\vec{r}, \hat{\Omega}', E'). \quad (2.2)$$

Even after eliminating half of the terms in Eq. 2.1, Eq. 2.2 is an integro-differential equation with terms in six dimensions: three in space, two in angle, and one in energy. Typically, problems with this level of complexity are not solved analytically and, in fact, a traditional mathematical solution may not even exist for some systems that this expression describes [11]. Eq. 2.2 must then be solved numerically, and as the topic of this thesis is not pioneering methods of solution for the transport equation, with an established set of computational transport methods.

In order to numerically solve Eq. 2.2, the dimensions that this expression is evaluated upon must be discretized. Spatial discretization is fairly straightforward as three dimensional meshes are commonplace throughout engineering with complex geometries able to be approximated quite closely [11]. Many algorithms have been developed to create meshes with required or desirable qualities for specific solution methods, but the general idea of discretization in space is to divide the continuous space in which a partial differential equation needs to be solved into distinct sections [11]. Each vertex, edge, face, and cell that the space is divided into is required to have finite and quantifiable position, length, area, and volume respectively that the solver then utilizes to apply boundary conditions and solve the specified problem

[11].

The approach to energy discretization is significantly more narrow in applicability than the geometric considerations discussed above, but the concept is eminently similar in that the continuous energy spectrum is divided into finite bins or groups from zero to the upper limit of the highest energy group [14]. The multigroup method divides the energy spectrum into these groups depending upon the analysis being performed; both the number of groups and the energy at which group boundaries are established depend upon the problem of interest [14]. Generally the higher resolution in geometry, the fewer energy groups are needed to characterize large-scale particle behavior in transport simulations [14]. For example, full core neutronics simulations

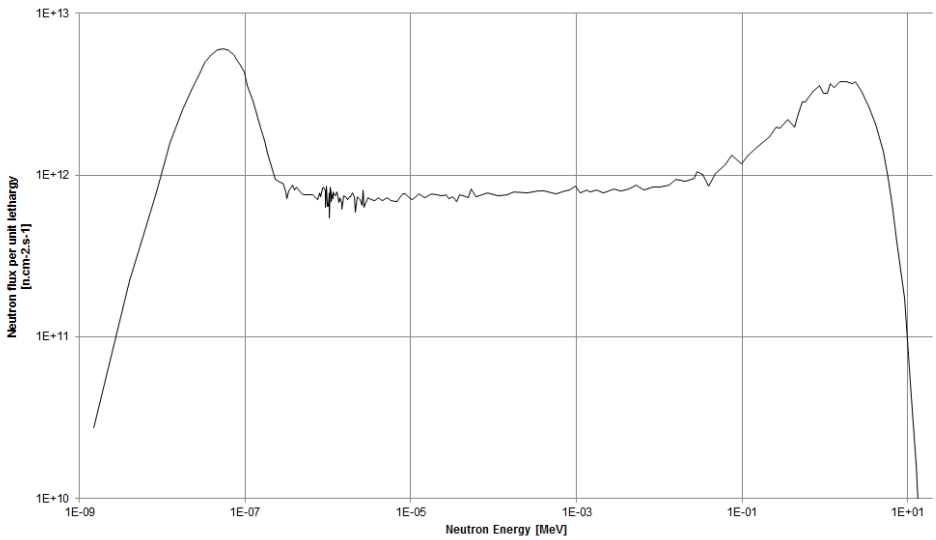

Figure 2.1: Flux spectrum of the NSC TRIGA reactor provided by the facility's engineering group.

typically contain three groups corresponding to the three regions with similar behavior evidenced in thermal reactor designs, yet reactor flux calculations consisting of a

single pin in an infinite lattice can contain hundreds of energy groups [14]. See Fig 2.1 for the identifiable energy regions in typical thermal reactor spectrums: thermal, epithermal/slowing down, and fast regions. In order to properly numerically evaluate flux in a system, it is necessary to collapse the continuous energy spectrum into energy groups, but this means that interaction cross sections which also depend upon energy must be processed to be used along with the group structure established for the rest of the problem [14]. Methods for collapsing continuous neutron interaction cross section distributions into discrete energy group dependent cross sections are detailed in Section 2.1.2: Cross Section Processing.

With physical space and energy in a problem now able to be used discretely in numerical approximations, angular effects must be considered. Neutron direction in

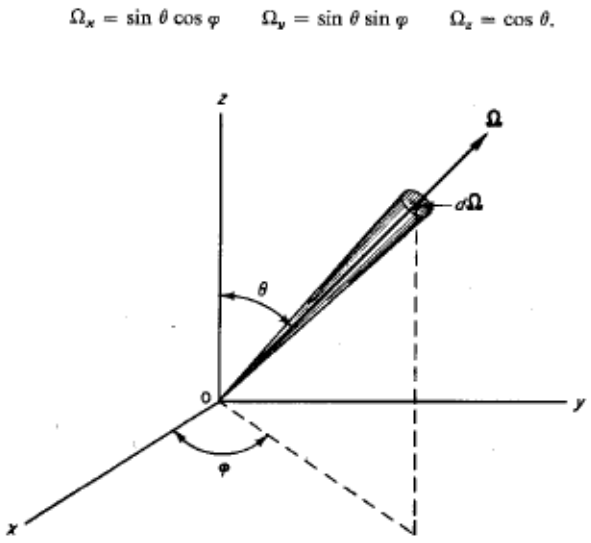

Figure 2.2: Solid angle visualized [8].

transport theory is prescribed by solid angle where in a three dimensional Cartesian

coordinate system, the polar angle is the angle of a specified dimension's direction typically on the x-y plane, the azimuthal angle is angle from the direction orthogonal to the surface that the full angle's projection is specified as the polar angle, and a delta angle to encapulate all angles in the cone of direction (see Fig. 2.2) [8]. To discretize this continuous angular specification, the solution method need be considered. The discrete ordinates uses angular quadrature to numerically approach integration over angle meaning that flux in solid angles is grouped into the most closely matching angles in a particular quadrature set [14].

With an understanding of how each dimension is expressed within the numerical evaluation, the strengths of the method are detailed. A major advantage of the discrete ordinates method is that it is a deterministic evaluation, essentially relating the first principles (Eq. 2.1) to the solution method. This is expedient as no features of the solution are assumed as they would be in probabilistic transport evaluations. To demonstrate this advantage, Monte Carlo, a commonly employed probabilistic method for obtaining solutions to transport problems, is briefly discussed. Transport solvers that use Monte Carlo track particles' behavior based on probabilities derived from interaction cross sections [14]. This is advantageous as sampling and decision trees are relatively computationally inexpensive but introduces additional error from sampling statistics in addition to requiring a large enough number of particles to track to successfully capture features of the flux solution [14]. A sufficient number of these particles can be upwards of many millions or billions to obtain a solution that in itself is only an approximation [14].

This method is also useful in that it solves the unadulterated transport equation (Eq. 2.1) rather than an approximation. The prevailing approach to numerical neutron transport for many years has been to use diffusion approximation methods as they reduce the order of the problem to be solved by eliminating angular con-

siderations [8] [14]. To arrive at this reduced dimensional method, the first order Legendre polynomial expansion of the transport equation in angle is found to be a diffusion expression, then Fick's Law applied to obtain neutron currents [8]. The exclusion of the two angular dimensions makes solving this problem much easier, but the diffusion approximation relies upon several assumptions about the system of interest; namely, that the scalar flux in this system is sufficiently weakly dependent upon angle, there is no material present with a high absorption cross section, and that material properties do not change abruptly [8]. In the large irradiation cell, the scalar flux is highly dependent upon angle as the source of neutrons in the cell is exclusively through the western wall with the reactor only several inches away and features of the cell including support beams and the lead experiment cart would be considered abrupt material changes from air, making codes that employ the diffusion approximation not ideal for the problem at hand.

While deterministic transport has many advantages, the reason that extensive computational resources have not been invested into this solution method until recently become apparent when attempting to solve a high resolution system. A multidimensional system of unknowns must be solved for each energy group; so even at relatively low resolution, the angular flux matrix can be massive [14]. Even solution methods such as source iteration that eliminate the need to store angular fluxes have a considerably large computational cost [14]. It is no surprise then that probabilistic approaches and diffusion approximations have been (and to a large extent in industry, still are) used as informative low cost evaluations for systems with high resolution geometries or finely spaced energy groups [14]. The complexity of this solution method is mitigated by a combination of better numerical methods, more efficient usage of computational resources with parallel algorithms, and powerful computer hardware.

In addition to computational complexity, another issue with using the discrete or-

dinates solution method for radiation transport is the method's angular dependence. In translating continuous angles to angular quadrature sets, unique errors arise in the solutions obtained using this approach. Ray effects arise due to the angular component of transport solutions being limited to angular quadrature set points and their origin can be shown to be related to differences in the spatial component of the discrete ordinates equations and corresponding spherical harmonics equations [12]. This error is often characterized by large differences in angular flux within a small volume that does not reflect a neutron transport problem's diffusive nature [14]. This error can be mitigated by using higher order quadrature, which increases problem complexity, but getting closer to a solution that reflects reality is worth the computational cost [14].

While measuring flux, specifying geometry, and identifying materials for an experiment that informs simulations is relatively simple, collecting angular data can be difficult for problems not utilizing collimated beams of radiation. With the source of neutrons in the irradiation cell being the reactor, a proper analysis needs to be informed by a neutronic model of reactor emissions placed within the problem's geometry to quantify emission angle. To overcome this obstacle, NSC engineering staff provide access to reactor models which are used in conjunction with validation data collected to optimize the reactor's position then determine the angular distribution of neutrons incident upon the face of the cell.

With an understanding of the discrete ordinates (S_n) solution method, it is now sufficient to say that there is enough confidence in numerical solutions to the transport equation (Eq. 2.1) using this method that providing boundary conditions acquired via experiments to a discrete ordinates code should yield an accurate characterization of neutron flux in this space. Given the boundary conditions and material properties of the space within the large irradiation cell, the flux solution obtained

from this method is taken as the model of the cell to be compared to experimental results. By perturbing the information provided to the code used to calculate the flux solution, uncertainty in the solution is identified.

2.1.2 Cross Section Processing

Specification of the material composition within the system of interest is required to provide the neutron transport solver with interaction cross sections. These cross sections are a property of materials which give the likelihood of a particle interacting with elements in that component via how large of an area the neucleus is perceived to be from the free particle's perspective [19]. An effective cross section may be calculated for materials consisting of various basic elements based on the abundance of these elements, but each interaction solely consists of the incident particle and the nucleus of a particular atom [19].

Cross sections are not static material properties. In addition to depending upon the material (thus being dependent upon the the spatial position of the materials in a problem to be solved), cross sections also rely upon particle track angle, and energy [19]. Determining the distribution of materials within a system is derived from the location of the various features in the geometry. Typically, meshes are created with the components and structures of the problem modeled such that each element has homogeneous material properties, with techniques employed for complex geometries to smear properties across elements with heterogenous materials [11]. Cross sections' dependence upon particle track angle arises in large crystalline structures as a particle travelling in a direction parallel to the structure's bonds may rarely interact with atoms while a track perpendicular to crystallographic planes is much more likely to allow the incident particle to interact [19]. Often, materials of interest are non-crystalline, in which case, cross section's dependence upon angle is generally

weak enough to neglect angular considerations [19]. Energy dependence proceeds from quantum mechanical considerations, but there are no empirical relations for these correlations [19]. Cross section spectrum data is derived from experimental observation and expressed in large data libraries such as Evaluated Nuclear Data Files (ENDF) [14].

For the irradiation cell, the angular dependence is neglected; so cross sections are determined by position and neutron incident energy. Creating the mesh with material blocks for the different features of the cell requires little in the way of theory, and this work is detailed in Section 4.1: Discretizing Geometry and Distributing Material in Cell. Energy dependence of cross sections relies on the discretization method. Having already examined the multigroup method, the theory of determining group averaged cross sections for the this scheme bears further description.

The energy bounds of each cross section group are already determined by the multigroup discretization, and an expression for the calculation of group averaged cross sections,

$$\sigma_{\mathrm{g}}(\vec{r}) = \int_g dE \ \frac{\sigma(x,E)\phi(x,E)}{\phi_{\mathrm{g}}(x)}, \tag{2.3}$$

arises from the multigroup derivation of the transport equation [14]. Cross sections are listed at specific energies rather than as an expression in nuclear data libararies; resulting in the need for an expression to approximate the integrals numerically.

$$\sigma_{\mathrm{g}}(\vec{r}) = \frac{\sum\limits_{j\in \mathrm{g}} \phi_j \sigma_j}{\sum\limits_{j\in \mathrm{g}} \phi_j}, \tag{2.4}$$

provides the approximate evaluation of a group averaged cross section [14]. This expression presents an immediate problem, as not only is the quantity attempting to be evaluated (scalar flux) required in order to calculate the group cross sections,

but the scalar flux must be known at least at the same energy values that continuous cross sections are listed in the cross section library.

One approach to this problem is to use a reactor theory informed flux spectrum due to the flux terms effectively act as weighting terms for cross sections at distinct energies in Eq. 2.4 [14]. A typical relative flux spectrum may be constructed by specifying limits for three energy group regions, then applying reactor theory flux spectrm behavior relations to the energy group regions [14]. Customary behavioral traits for energy regions in thermal reactors are a Maxwellian for thermal region, 1/E for slowing down region, and Watt-fission spectrum for fast region as evidenced in Fig. 2.2 [14]. If available, group averaged cross sections may also be calculated using the measured or modeled flux spectrum at an experimental position of interest to provide energy dependent scalar flux to Eq. 2.4 [14].

Each set of group averaged cross sections is only applicable to the data provided from the cross section library. Generally, cross section data is only specifed for isotopes; so to determine cross sections for each material, the group averaged properties first need to be weighted in proportion to their presence in the material's base elements then the elements weighted to their proportion in the material [14]

$$\sigma_{\mathrm{g,m}} = \sum_{i \in \mathrm{m}} w_i \sigma_{\mathrm{g},i}. \tag{2.5}$$

The group cross sections for the materials may now be supplied to the transport solver to use in the system's solution.

2.1.3 Neutron Activation Analysis

With the discretized transport equation and processed group cross sections, everything needed to compute general flux solutions is known, but flux incident upon the cell and within the cell is necessary to develop the problem's boundary condi-

tion and validate the cell model respectively. Five of the six walls of the irradiation cell have zero incident neutron flux as there are no radiation sources beyond them, but the wall facing the reactor pool acts as a boundary source of neutrons into the cell; so the incident flux magnitude across the face of the wall needs to be known. The model also needs to be validated against flux measurements within the cell to demonstrate that the results of the computed flux accurately reflect the behavior of neutrons during irradiation cell experiments. In both cases, the need for a method of gathering flux measurements is apparent.

Neutron activation analysis is a process by which a sample's elemental components are identified by irradiating the material with a neutron source [19]. The natural elements in the sample with sufficiently large neutron absorption interaction cross sections will have atoms that absorb neutrons to be transmuted into radioactive isotopes [19]. Many of these radioisotopes emit gamma and beta radiation at discrete energy values which can be used to identify them and thus the original elements within the sample [19]. While this technique is useful for identifying chemical elements present in a sample of unknown composition, it is employed here for its ability to distinguish the level of activation an isotope has received [19]. The neutron activation equation

$$A(t) = \frac{\sigma \phi N_o}{\lambda} \left(1 - e^{-\lambda t_{irr}}\right) e^{-\lambda t_{decay}} \tag{2.6}$$

can calculate a sample's activity a given amount of time after the sample has been irradiated using the original isotope's mass and cross section, the radioisotope's decay constant, neutron flux at experimental position, and amount of time the sample is irradiated [19]. By rearranging Eq. 2.6, the neutron flux can be calculated from the sample activity, which is quantifiable by counting the sample on any detector capable of energy discrimination with a multichannel analyser [19]. Detailed in Section 2.2.2,

high purity germanium counters and associated equipment are able to perform this type of analysis and are available at the NSC for experimental use.

The question as to what sample to use with NAA to calculate flux at points throughout the cell remains. Flux foils are commonly employed for this this purpose, and the NSC allows experimenters to use gold-aluminum flux foils the facility has on hand. The foils are thin, circular and sized at less than a centimeter in diameter effectively allowing their flux evaluations to be recorded as point measurements in comparison with the scale of the cell. Gold is an attractive option as a flux measuring

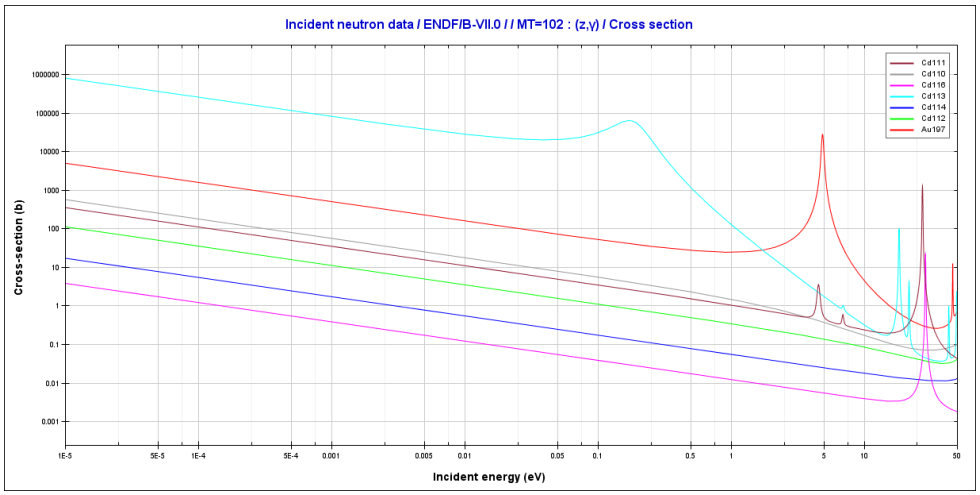

Figure 2.3: Plot of Au-197 and cadmium natural isotope radiative capture cross sections versus incident neutron energy generated with JANIS.

sample for low energy neutrons due to it's larger than average thermal cross section and kink in the low epithermal range as evidenced in Fig. 2.3. However, due to the cost of gold, it should not be surprising that facilities are hesitant to shop at the local jewlery store for experimental supplies. Instead, foils are comprised of a small amount of gold (0.127% by mass for the NSC's foils) dispersed throughout aluminum

sheets with a ratio maintained between the two elements to ensure the mass of gold is consistently proportional to the total mass of the sample. The gold-aluminum foils maintain gold's ability to capture neutrons without adding a lot of additional activity to the sample as aluminum has a relatively negligible neutron capture cross section in comparison [7].

The appeal of using gold because of its cross section has already been detailed, but in order to define and discriminate between epithermal and thermal neutrons at a foil's location, a sandwich of foils is to be used. One bare gold-aluminum foil and one covered foil are prepared together to place at each experimental location. Desirable properties for the covered foil include being thin enough to encapsulate the foil without the foil being able to move and the foil's material needs to have a cross section able to screen out one of the energy groups. Cadmium is a good candidate as Cd-113 (12.22% natural abundance) has a radiative capture cross section several orders of magnitude higher than gold in the thermal energy region while most of cadmium's natural isotopes' cross sections are much lower than gold's in the epithermal region (with a few exceptions being fairly narrow energy resonances) [7]. With one foil absorbing neutrons in both energy regions and the other only primarily recieving epithermal dose, the flux in both energy regions may be determined.

2.2 Experiment Equipment

An overview of the tools and equipment utilized in experiments is necessary to understand their effects within the study. Each summary aims to give a brief description of the tool or technical specifications in cases of equipment used, its primary use, and what capabilities are employed in this work. Also provided when necessary are which tools each will interact with specifically focusing on what input and output are required going to or from each tool interaction.

2.2.1 Nuclear Science Center Reactor

The Nuclear Science Center Reactor is a one MW pool-type TRIGA with low-enriched uranium (LEU) 30/20 fuel and two operational states able to irradiate samples in various configurations [2]. The reactor may operate in steady state or pulse (transient) modes due to the inclusion of a high worth transient rod, and it is designed to utilize several unique experimental locations such as the large irradiation cell and beam ports by having the reactor support structure upon a movable bridge [2]. Principal safety features include passive shutdown capability and negative temperature reactivity feedback [2]. Reactor power is controlled with four shim safety rods, a high reactivity worth transient rod, and a low reactivity worth regulating rod. Detectors to monitor power include compensated (linear channel) and non-compensated (safety channels) ion chambers as well as a fission chamber (log channel) [2]. Fuel temperature is collected from specially designed instrumented fuel elements with thermocouple leads embedded within each element at three axial locations [2]. Experiments are often positioned on the west face of the core in tubes that fit over bayonets at grid positions in the A row, but two in-core positions at grid locations D3 and B1 allow west face tubes and pneumaticly inserted samples to be irradiated respectively [2].

As the Nuclear Science Center's reactor is a TRIGA (Training, Research, Isotope production, General Atomics), the facility has always strived to have its operational policies in line with the reactor's acronym. Several laboratory classes at undergraduate and graduate levels offered at Texas A&M University allow students to get hands on experience operating and experimenting with this research reactor, and operator training for commercial plants in Texas has been conducted at the NSC [2]. The NSC allows academic and non-academic use of the reactor for research with many

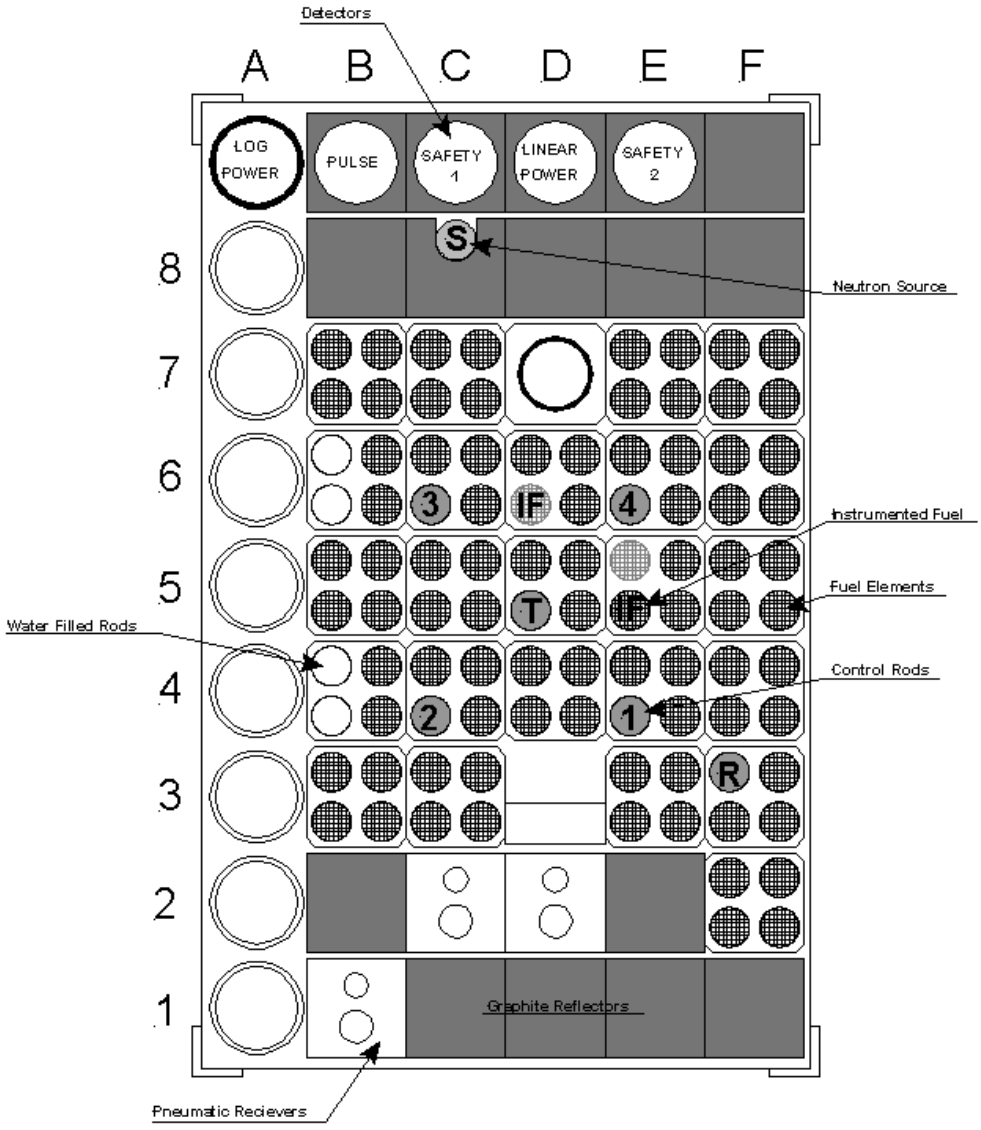

Figure 2.4: NSCR current core configuration [2].

experimenters from research programs at Texas A&M and industry leaders such as Lockheed Martin. Much of the commercial operation at the facility comes from isotope production useful in medical and energy applications.

To study the characteristics of neutron transport in the irradiation cell, the re-

actor acts as a neutron source. Experiments on the west face of the reactor are removed and a void box installed to maximize neutron dose inside the cell [3]. The reactor is then positioned on the far west side of the pool just outside the irradiation cell's window after the appropriate safety checks have been performed [3]. During irradiation cell experiments, neutrons stream into the cell's volume from the cell window. Depending upon experiment dose requirements, samples may be placed in a variety of locations in the cell including the movable lead box on a rail system in the center of the room. The irradiation foils used to collect flux in this study are mainly placed on the window's surface to collect data for neutrons incident upon the cell's volume, but foils collecting validation data are placed at a variety of spatial positions throughout the cell.

2.2.2 High Purity Germanium Detector

To perform neutron activation analysis, gamma emissions from the irradiated foils must be quantified in energy to develop peak counts on an energy spectrum. This requires a detector capable of discriminating gamma emissions' energy deposition in an interaction, a multichannel analyser to sort each interaction with the detector into energy bins depending on the energy deposited, and software designed to compare experimental input with gamma peak data and perform statistical analysis to provide results with uncertainty [19]. High purity germanium detectors are high resolution inorganic scintillators housed in a vacuum packed crystat unit [19]. By promoting electrons from the valence band into the conduction band of the crystal, positive holes ionize activator sites and electrons caught decay with visible photons after a charged particle interacts with the crystal [19]. By quantifying the amount of light recorded for each interaction, the energy of emissions is characterized [19]. By comparing the peak counts recorded to radioisotopes' known gamma emissions, the probability

that a particular isotope is present in a sample, activity of a particular isotope, and experimental uncertainties in quantities of interest can be quantified [19].

The Nuclear Science Center offers NAA services to researchers with the onsite counting lab. The detector type used in the counting lab for isotopic analysis is high purity germanium for its fine and accurate energy discrimination and proven reliability as an industry standard tool. Several HPGe detectors are utilized in conjunction with CANBERRA Industries' Genie 2000 spectroscopy software to determine the current activity of ^{198}Au. Using relations in the NAA theory section with experimental data and the results from the counting lab, the neutron flux and measurement error is determined at a flux foil's experimental position.

2.3 Computational Tools and Resources

2.3.1 Parallel Deterministic Transport (PDT)

Various neutron transport tools are in use throughout the industry, but many are probabilistic in nature or only offer solutions in simple geometries with processing constraints. The Parallel Deterministic Transport (PDT) project was started in 1998 and solves the discrete ordinates transport problem using efficient sequential algorithms distributed amongst parallel cache-based computational systems [5]. The code is massively parallel, scaling on logically Cartesian grids out to 750,000 cores [5]. It can solve multigroup, criticality, and depletion problems in steady-state and with time dependence [5]. PDT has several radiation transport models including those for neutrons, photons, and electrons as well as coupled modes for neutron-gamma and electron-photon transport. [5]. PDT has shown steady progress in development, and neutron transport is a continuous topic of interest. Using this tool as it is in development will serve to validate its predictive simulation capabilities for our problem.

PDT does all of the heavy lifting with regards to characterizing the neutron flux distribution throughout the cell. As a first-order transport solver, it requires a mesh to solve upon, several material properties, boundary conditions, and localized sources to be provided. These are all developed throughout the course of this work either via measurement (the cell's physical characteristics and neutron flux at various positions to inform boundary condition) or research (identifying cell construction materials, finding material chemical compositions and densities). PDT uses the provided input to numerically calculate flux throughout the problem and returns volume averaged scalar flux, flux through each cell's surface, and (optionally) silo files to visualize results. Cell averaged scalar flux values for cells corresponding to flux foil locations will be the quantities of interest from the model compared to foil experiment data.

2.3.2 Python Programming Language

Python is a programming language developed with extensibility in mind [20]. It is used extensively for scientific programming applications due to its intuitive nature and standard control flow tools [20]. Most of it's implementations compile at runtime with inheritance accomplished by importing modules with functions for a script to use [20]. Python is often distributed with many modules that allow the language to flexibly interact with computing environments and perform various specialized tasks [20]. Its commonly used compound data type (lists) is versatile, but not suited for operations in linear algebra; so Numpy arrays are substituted when necessary [20] [6]. Numpy is a scientific computing package capable of storing data in N-dimensional arrays, performing linear algebra, sampling random distributions, and integrating C, C++, or Fortran code into Python [6].

Python and numpy are used for various data manipulation and analsys throughout this work. Cell discretization, mesh development, cross section processing, an-

gular determination, PDT input file generation, and the heron validation framework were all developed using Python and Numpy. The scripts are executed in a specific order to produce PDT input and extract output for analysis. In the series of computational tools used to produce results, flux fitting, solution of the transport equation, silo file visualization, and cross section generation are the only processes that do not use Python; so the extent of its use cannot be understated.

2.3.3 R Project for Statistical Computing

R is a programming language primarily used for statistical computing [18]. It supports linear and nonlinear modeling, clustering, classification, and statistical testing and, like Python, is highly extensible through the use of function packages and linking with languages used such as C, C++, and Fortran [18]. R can also produce publication-quality static graphics and supports matrix arithmetic [18]. It is of interest to this work for its extensive regression models and ability to quantify standard errors for models produced [18]. Flux values calculated from foil activities on the window are read into R and fitted to a surface to approximate flux magnitudes across the irradiation window. R can also provide nominal flux values over the fitted surface as well as the fit's standard error at any point from the surface which provides confidence envelopes to sample from when needing to perturb the cell's boundary condition.

2.3.4 OECD Janis

Two material properties need to be provided to PDT for it to calculate the macroscopic cross sections necessary to evaluate the transport equation: material density and group-averaged cross sections. Density may be easily found or calculated, but neutron cross sections are more difficult to quantify when dealing with a distribution of energies. A commonly used tool for obtaining cross section data for materials is

OECD's Janis software. Developed as a Java application, it allows users to specify materials and interactions then searches for cross section libraries that match the user input [17]. Cross section data preparation and visualization are made easy in Janis with tables able to be exported to common file formats such as comma separated value (csv) or MS Excel [17].

A csv file containing scattering and total cross sections for each isotope present in materials in the cell is generated using JANIS. These csv files list the cross section by incident neutron energy and must be processed into group averaged material cross sections using the reactor's flux spectrum and energy group bounds determined by the flux foils. Natural element isotope distributions and elemental abundances in materals are then used to determine the cross sections for materials to be provided to PDT.

2.3.5 LLNL Cab

Thanks to the Predictive Science Academic Alliance Program (PSAAP II), students from participating universities may utilize unclassified computing resources from a the Tri-Lab partnership of US national laboratories Lawrence Livermore, Los Alamos, and Sandia [4]. PDT is an export controlled code limited to installation on licensed systems but solves for the spatial resolution the irradiation cell models require are computationally expensive; so having access to computing resources both secure and powerful makes studies such as this possible. Lawrence Livermore's Cab machine allows LLNL collaborators access to 1,296 computing nodes each with 16 cores and 16 Gb of memory per core; running at a peak of 431.3 TFLOP/s [4].This machine is used to run all PDT simulations taking advantage of the code's parallel nature and Cab's extensive resources to reduce the walltime of validation runs to a reasonable level.

2.3.6 VisIt

VisIt is Lawrence Livermore National Laboratory's open source visualization and analysis tool [9]. It allows users to visualize data, animate visualizations in time, and manipulate data via operators [9]. VisIt can generate plots from a variety of mesh types including structured, adaptive, and unstructured meshes in multiple dimensions (2D and 3D) [9]. The tool is also very flexlible, being able to visualize data in parallel scaling up to the use of cores on the order of 10^5 and being able to visualize data from over 120 different scientific data formats [9]. As PDT outputs to silo files that VisIt is able to use, this tool works to verify cell geometry and visualize PDT flux solutions throughout the cell.

3. DATA COLLECTION

The advantages of collecting data from experiments include using results to inform simulation inputs and validate the computational model's results. However, the nature of experimentation introduces error into the results. In the following section, experimental setup procedures are discussed including methods of reducing experimental uncertainties and quantifying uncertainties that are available. The data collected falls into two broad categories based upon where in the study data points are utilized. While the data collected is all measured in the same way, each collection point's use is dictated by whether the point is on the cell's window. Flux data from points collected on the window are fit to a surface and used as the nominal flux distribution for each energy group. This is one of the first steps to devleoping a boundary condition to provide to PDT. The standard error of the fitted surfaces also specifies the standard deviation used in sampling to quantify the uncertainty in the PDT model. Other points collected inside the cell provide validation data for the computational model once run and are used as a measure of how closely the model resembles the reality of experiments.

3.1 Experiment Setup

Before setting up experiments in the large irradiation cell, several safety measures must be taken. The reactor bridge's west side must first be at least six feet away from the side of the pool that shares a wall with the cell [3]. This is ensured by a locked rail stop just beyond this distance preventing the reactor bridge from moving past that point as well as a cord that is only unplugged to trigger an interlock preventing the motor driven shield (see Figure 1.1) from being opened if the reactor is beyond the six foot safety distance necessary for irradiation cell operation [3]. A series of checks

performed before reactor startup additionally ensures that reactor operation above 100 kW allows the reactor operator on duty to limit access to the lower research level as cell operations can raise background radiation levels to those only acceptible for certified radiation workers [10] [3]. A locked power box is turned on to move the motor driven shield then turned off and locked again ensuring any reactor movements will prevent startup while the cell is open. A portable ion chamber detector is lowered into the cell establishing the safety of background radiation levels in the cell. With the approval of the senior reactor operator and a member of health physics staff, the experimenter may now enter the cell.

A ladder is then lowered with a winch into the experiment area. A radiation worker climbs down a permanent ladder to the upper portion of the cell then down into the experiment area in the lower cell via the lowered ladder. At all times, the experimenter has both the key to the power box for the motor driven shield and a walkie talkie to communicate with the control room. Once the experiment is set up, the process is repeated in reverse to end up with the experiment in the cell with the shield covering the cell and power box locked in the off position.

With the experiment ready for irradiation and reactor shut down, all samples are removed from the west face of the core and a void box installed to facilitate maximum exposure of samples to neutron dose. The western pool side rail stop is removed and proximity interlock cord unplugged from the reactor bridge. The bridge is then carefully raised and moved to the irradiation cell's window. Lines for the transient rod's pneumatics and reactor instrumentation must be moved to accomodate the bridge's new position. To mitigate positional changes in the reactor's location in relation to the cell, the reactor bridge must be positioned as consistently as possible for each experiment. To ensure this regularity in the reactor's position, the reactor bridge's offset from the pool wall is placed at a set position for each experiment. Even

accounting for the consistency of the bridge's placement, the reactor's position has a small amount of uncertainty due to lowering the reactor's structural components to seat the system before startup.

The reactor is started up to the desired power level while monitoring area radiation monitors throughout the facility for unexpectedly high emissions. Each experiment is run at one megawatt for fourty-five minutes to provide adequate dose without achieving saturation activity in the small amount of gold in the foils. Due to operational availability and the nature of experiments in the irradiation cell, data collection occurred over a period of several months, during which the changes in flux distribution dosing the cell are uncertain. To relieve some of the short term fluctuations, experiments are conducted only when reactivity poisons, most significanly xenon, have decayed away by collecting data only after at least two days of the reactor being shutdown.

In order to assure the reader of the replicability of these experiments, sources of experimental error and the methods to mitigate them are discussed. Sources of uncertainty in running the experiments include the manual positioning of the reactor on the west pool wall for each experiment and the reactor's neutron flux profile changing throughout its operational history. The positional changes are limited by the reactor bridge's consistency in location, and operation is kept as consistently as possible by limiting experiments to first startups at least two days after the last reactor operations to limit the buildup of fission products that negatively impact reactivity (short lived fission product poisons) [2]. To limit inadvertent neutron dose after the experiment, the reactor is promptly shut down and immediately moved to the opposite end of the pool after the experiment.

3.2 Foil Placement Methodology

As neutron flux magnitude fit surfaces are required to develop the simulation's boundary condition, point collection on the window is given priority. Each experiment utilizes a different pattern of flux foil positions on the window with several points chosen to collect replicate data from positions previous monitored as an indicator of consistency of dose on the window. Patterns are chosen randomly by the experimenter, but as evidenced from Figure 3.1, there is a certain regularity and symmetry to the data points collected on the window. Perhaps sampling the space with latin hypercube or stratified sampling techniques would provide more even distribution of data, but with the number of original sample positions well over eighty, the window's area has been sampled adequately to develop a surface fit of flux with relatively small error.

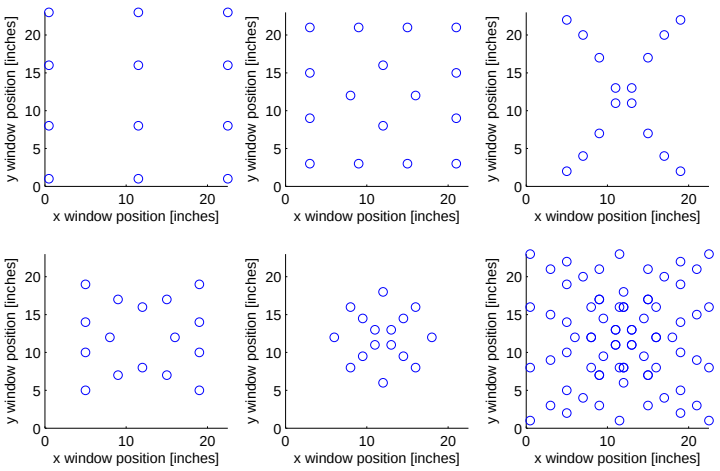

Figure 3.1: Foil placement on the cell window and all foil positions in sixth plot.

Validation data is collected from various points throughout the cell. Again, the experimenter's whim was the only sampling technique utilized in distributing foils throughout the cell, with foils typically being mirrored across the midplane perpendicular to the north and south directions in the cell. Data is collected within line of sight of the window, behind the structural beams, on the wall shared with the pool, the north and south walls, and a few points collected on the floor.

3.3 Counting Foils

After around 30 hours, the lingering radiation from activation of structural materials decays away, and the flux foils are able to be safely collected and counted. The safety procedure detailed in Section 3.1 is repeated to gain access to the cell and foils extracted. Each is labeled, weighed, and counted on the NSC's high purity germanium detector. Five minute counts are taken for each foil and a report generated detailing the activity of various elements in the sample. The neutron activation equation is rearranged to solve for total flux of the foil at this position depending upon the energy groups it encompasses:

$$\phi_{\text{epi}} = \frac{A_{\text{covered}}}{N_o I_o (1 - e^{-\lambda t_{\text{irr}}})} \tag{3.1}$$

$$\phi_{\text{therm}} = \frac{\frac{A_{\text{bare}}}{N_o(1-e^{-\lambda t_{\text{irr}}})} - \phi_{\text{epi}} I'_o}{\sigma} \tag{3.2}$$

The cadmium covered foil need only utilize the epithermal cross section, but the bare foil accounts for both the full range of gold's absorption spectrum (i.e. low energy epithermal and thermal energies), so the calculated epithermal flux is factored into the thermal flux's expression. This is done with a spreadsheet for all foil pairs in each experiment.

Experimentally determined flux results are listed in Appendix B listed by a mea-

surement point ID. The cell locations of these location ID's are found in Appendix A. Bolded entries are used as validation data, while the rest is used to construct the model using window data. By plotting the window points by position and flux magnitude, it may already be observed that a mound-like shape is observed for both energy groups with larger flux towards the center of the window and lower flux levels at points on the edge, giving futher confidence that a surface fit model will be able to model the reality of the experiments with this regular shape of the results.

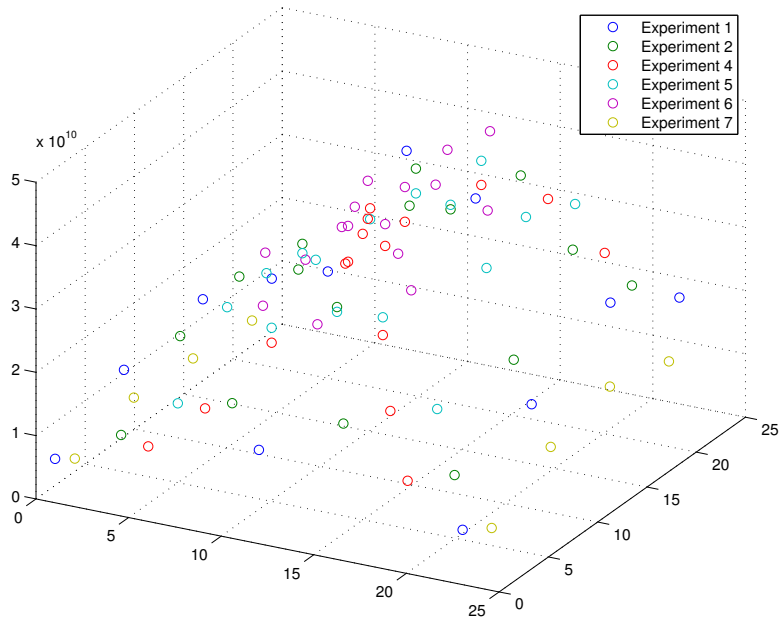

Figure 3.2: Scatterplot of calculated epithermal flux on cell window.

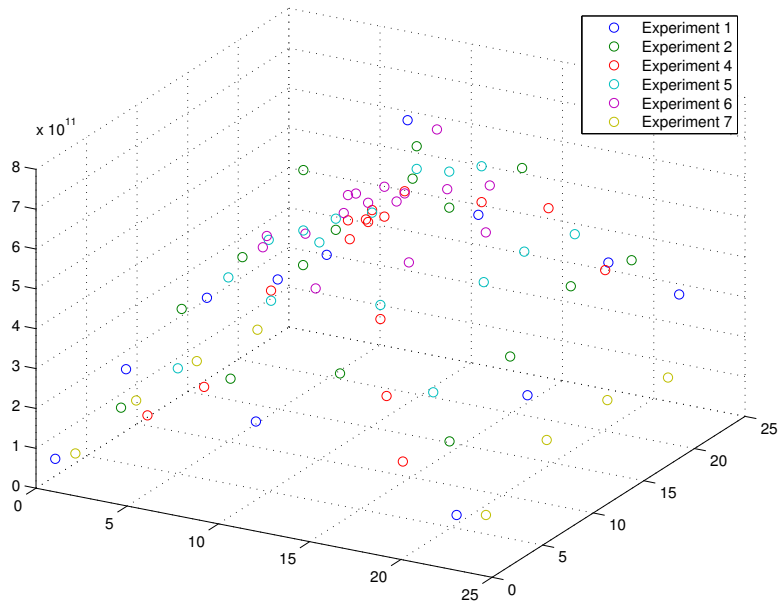

Figure 3.3: Scatterplot of calculated thermal flux on cell window.

4. MODEL AND VALIDATION FRAMEWORK CONSTRUCTION

In order to create a computational model of the irradiation cell experiments performed, a series of scripts are developed in Python and R languages with interdependent output to provide as input to PDT. The simulation will require three aspects of the experiments to run: the cell's geometry, cell material properties, and a boundary condition that approximates dose from the reactor. The boundary condition is the most involved to calculate as flux on the boundary is specified by position, by angle, and by energy group. The energy groups for the boundary condition are determined by the data collection scheme as the epithermal and thermal regions are separated by the bare and cadmium covered foil method with an energy cutoff between the groups at 1 eV, but the cell's material data, namely absorption and scattering cross sections, must be processed to provide group averaged values to PDT. The mesh is created from physical measurements of the cell and constructed using PDT's block mesh generator.

4.1 Discretizing Geometry and Distributing Material in Cell

A discrete representation of the cell must be developed to specify the geometry of the problem. Physical measurements of the cell are easily surveyed with a tape measure and the various materials in the experiment space identified from facility documents such as the Safety Analysis Report [2]. PDT's bundled regular Cartesian three dimensional mesh generator is chosen to creates a block mesh of the cell. While most features in the cell are conveniently able to be accurately approximated with a block mesh, the slant of the concrete wall around the window must be estimated with a stepped geometry.

Cell measurements are first separated into blocks that represent regions of one

type of material. These regions have consistent geometry, but are later divided into smaller cells to mesh the problem. A spreadsheet specifies each material block's name, material, and start/end points in each of the three spatial dimensions then exported as a comma separated value (csv) file. The steps representing the window slant material regions are calculated from a script to develop the stair stepped geometry approximation depending upon the desired spatial resolution of the simulation (i.e. higher resolution yields smaller but more numerous steps approximating the slants).

In order to mesh the problem, the spatial input to PDT is divided into cells with size dependent upon the division groups of each dimension the cell falls within and the resolution specifed for the simulation. Using a Python script, the material block data is read and geometric extents of each region separated into variables corresponding spatial dimensions. Each dimension's unique values are found then ordered to create the division boundaries between material regions.

The script continues on to discretize the dimensional divisions. Python dictionaries are created for the dimensional bounds for each division, and the resolution of the problem is specified at this point by indicating the number of cells in divisions. Parallel computing ability is also indirectly established at this point as the total number of cells in a dimension must be divided evenly amongst the number of processors available to the dimension. In developing the resolutions, arbitrary maximum cell sizes are established. For example, the 'fine' resolution has a maximum size of 3 cm in each dimension, while 'super-fine' increases the resolution to 1 cm for each dimension. The medium resolution mesh is used in final calculations due to it's relatively high resolution (maximum cell size of 10 cm, with average of about 7 cm) in comparison to the scale of the cell and the speed of calculation. With the number of cells in each division specified, another dictionary is created to assign sequential

numbers to each division's cells. A material region array is generated by matching the region extents from the read block data to the recently generated cell numbers in each dimension. This identifies the bounds of each material region from a beginning cell number in one spatial dimension to the last cell number in that dimension that material region spans for all three dimensions.

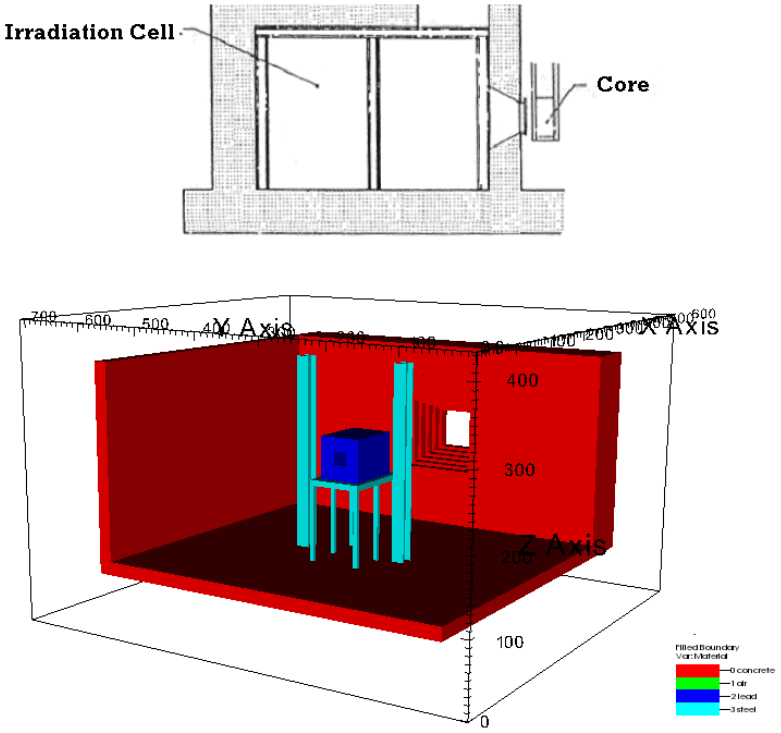

Figure 4.1: Comparison of generated cell mesh to original geometry [2].

This is all the information needed to create the mesh in PDT, and several output files are written. A file specifying characteristics for each division in the dimensions informs PDT spatial input to create the divisions specifying their start and end as

well as number of cells. The material region array with cell numbers is also written as PDT specifies the start and end cell numbers for each dimension as well as the material of the region. Two additional files are written to make certain aspects of the geometry more easily available to other scripts. Flux from the reactor is incident upon the cell's east wall; so the vertices on this wall are written to a file to aid in flux magnitude fitting. The extents of the window in the current geometry are also output for other scripts to use.

4.2 Material Properties and Neutron Interaction Cross Sections

With the cell meshed and material distributed spatially, properties for each material need to be enumerated, namely the materials' densities and group averaged cross sections. Four materials are found in the cell: air, high density concrete, structural steel, and lead. In addition, water and gold material properties must be specified for calculation of reactor optimization and foil processing respectively. Densities of the materials may be found in a variety of references, and cross sections are calculated depending upon the energy bounds of a problem. To construct the material cross sections, nuclear data for each isotope present needs to be processed; so determining the elements that constitute each material is also necessary.

Material densities and elemental compositions are found from a variety of resources. Some materials' elemental make up are obvious: gold, lead, and water; and their densities are easily found in tables of densities for natural elements [13]. Gold's cross section is processed independently from it's small weight percentage in the gold aluminum foils due to the nature of the calculations in which the cross sections necessary are utilized, and while some small impurities are no doubt present in the water, the reactor pool water purification system eliminates almost all contaminants to prevent inadvertently activated material in the pool [2]. Pool water is counted

every day after the reactor is started up to ensure consistent and safe operation [2].

The material data for high density concrete data is generated from a 1965 report from Oak Ridge National Laboratory [15]. As the construction of the NSC was begun in the late 1950's, the concrete used in construction of the NSC's pool wall and structure is likely very similar to the concrete analyzed in this report due to the more limited number of construction materials available for reactor facilities at the time [2]. The report details the elemental composition, densities, shielding data, and sources of materials used in the concrete [15]. Steel used in structural materials and the experiment table in the cell for the model has material properties specified from an American National Standard report on ANSI/ASTM 500 steel [1]. Both the chemical makeup and density of steel are specified. Properties for all other materials relevant to the cross section calculations, aside from cross section data itself (e.g. natural isotopic abundances), are found in the chart of nuclides [7]. Material densities and elemental composition are found in Appendix C.

Cross sections at various energy levels are required to calculate the group averaged nuclear data the simulations require. The Organisation for Economic Co-operation and Development (OECD) provides a tool to generate cross sections from publicly available nuclear data [17]. JANIS allows users to detail the material, incident radiation, and type of interaction to return the applicable data from vast libraries of cross sections [17]. All cross section data used in this study is taken from the ENDF/B-VII.0 libraries. Depending upon whether the material itself has data recorded in the library, cross sections are generated for either the material or individual isotopes present [17]. PDT will use the total absorption and scattering cross sections. The cross section energy bounds needed are limited by the energy bounds of the experiment then extracted from the library and saved as csv files.

A Python script uses the isotopic distribution of elements, atomic masses, and

energy bounds of the experiment to calculate the group averaged cross sections. The reactor's flux spectrum in energy (Fig. 2.1.1) as measured from the west face of the reactor and provided by NSC engineering staff is utilized by the script as well. A developed class takes the cross section file location for a given isotope, reactor flux spectrum, and energy bounds to calculate absorption and scattering interaction probabilities. The JANIS cross sections are then either interpolated or matched within a tolerance of 0.01 eV to the energy values where reactor flux spectrum data is available, and the flux spectrum separated into the two groups. Group cross sections are calculated by using numerical integration and cross section group calculation equation

$$\sigma_{\mathrm{g}} = \frac{\int_{E_{\mathrm{g}}} \phi \cdot \sigma}{\int_{E_{\mathrm{g}}} \phi}. \tag{4.1}$$

The group averaged cross sections for each element are then calculated by multiplying the isotopic distribution percentage of each isotope by the calculated isotope cross section and summing each of these products for each itsotope in the element. Finally, the material cross sections are calculated by the sum of the products of the atomic percentage of each element in the material with the element cross sections. The cross sections are output to material files for PDT as well as in a text file that explicitly specifies each cross section's value.

Table 4.1: Processed Neutron Total Group-averaged Cross Sections

Material	Total Cross Section [10^{-24} cm^2]	
	Gp 0	Gp 1
High Density Concrete	13.0368	15.5964
ASTM A500 Steel	11.0996	12.7948
Air	8.5895	9.5936
Lead Brick	11.1943	11.3180

Table 4.2: Processed Neutron Scattering Group-averaged Cross Sections

Material	Scattering Cross Section [10^{-24} cm^2]			
	Gp 0 $\rightarrow$ 0	Gp 0 $\rightarrow$ 1	Gp 1 $\rightarrow$ 0	Gp 1 $\rightarrow$ 1
High Density Concrete	2.7068	10.3081	0	15.2382
ASTM A500 Steel	10.2349	0.76309	0	11.1347
Air	6.4336	2.0996	0	8.6818
Lead Brick	10.9738	0.2139	0	11.2114

4.3 Surface Fit from Experimental Results

With the geometry and material properties of the problem defined, only the boundary condition is needed now to run PDT simulations. Experiment data is used to develop the condition by first using statistical techniques to fit a surface to the points which approximates the scalar flux for each energy group incident upon the cell's east wall from the reactor pool. Statistical fitting is used rather than an interpolation scheme so that the same surface may be used with a variety of geometric discretizations depending upon the developed spatial resolution of the problem. Regression based fitting can also generate confidence intervals from the residuals of the fit for allowing sampling of the flux at specified points which is useful in uncertainy quantification.

The R statistical computing environment is chosen to create the surface fits and compute confidence intervals. An R script is developed to read in experimental data and translate the experimental geometry to the simulation's spatial discretization. Vertices of the cells on the east wall are also read into the script and the extents of these points limited to just outside the edges of the window as the only experimental data collected is in this region; so extrapolating flux magnitudes outside of this domain would yield both larger error in the fit and a lower confidence that the

results reflect the physical characteristics of the experiments.

After exploring several fitting schemes, the linear Loess technique is decided upon over other surface fitting methods due to its higher R^2 value for both epithermal and thermal fits and localized smoothing properties. While many statisticians would argue that Loess is more useful as a tool to determine overall trends in the data rather than a method to model a physical quantity, the relatively low smoothing value, high R^2, and lower uncertainty than other techniques makes this method an attractive choice for this study. Surface models are created then arrays created of the nominal fitted flux values and standard error at region limited east wall vertices. The fits are plotted, and then two sets of data output for each energy group: the reduced extent vertex points with nominal fitted flux values and fitted flux values with the standard error at each vertex.

4.4 Angular Discretization

With flux incident upon the cell window at vertices now specified, the flux must be further divided into the angles that contribute to this flux because the flux on the window is not isotropic. Traditionally, this is a difficult task to do for experiments as only the total flux at a point is collected. As the reactor is the source of emitted neutrons, an approximation of radiation from the reactor is used in conjunction with collected validation data from inside the cell to optimize the reactor's position in relation to the cell.

With the location of the collection of source points estimating reactor emissions and the cell vertices on the east wall for the chosen spatial resolution, the reactor sources create a set of discrete angles for each wall point. In addition, the magnitude of the sources' strength allows for the creation of weights for the angles based on the ratio of the level of emissions coming through the point at a particular angle

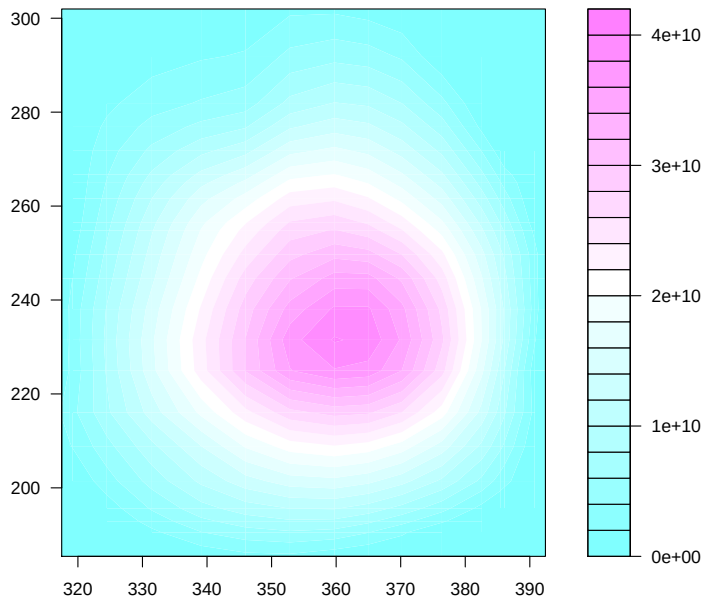

Figure 4.2: Lowess fit of epithermal flux on window viewed from pool

to the total source strength through the point. For PDT to use this, the discrete angles must be within a given angular quadrature set; so the discrete angles are matched with the closest angle in the chosen quadrature set and the weights added to the angle in quadrature at that point. The percentage of total flux at each point (the weights) applied to all angles that radiation passes through each point when multiplied by the fitted flux value at the point gives an angular-like flux for discrete angles.

4.4.1 Reactor Position Optimization

A point source reactor approximation is used to estimate neutron emissions from the reactor. This is derived from a neutronic model of the TRIGA created by NSC engineering staff to characterize neutron flux in and around the reactor's fuel bundles.

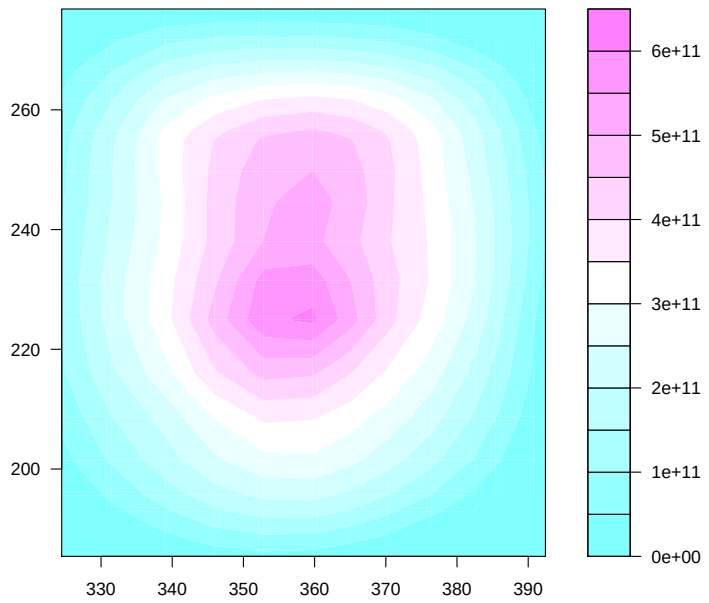

Figure 4.3: Lowess fit of thermal flux on window viewed from pool

Each fuel rod is represented as a series points with varying height. The series of fuel rod points collectively represent the reactor. Each point has an associated fission rate which is multiplied by the overall average number of neutrons produced per fission reaction to yield the activity of the point in neutrons produced per second. While a much more thorough analysis would need to be performed to get an accurate activity for these points in the reactor, recall that only the ratio of the neutron production rate is used to calculate weights employed in simulations.

A Python script performs the reactor position optimization. After reading in the source point and validation data, cross section data is also input. The optimization space is defined and each entry in each dimension of the specified optimization space is looped over. In the inner loop, an object is instantiated from the optimization

point and point approximated reactor data. When initialized, the object uses the optimization point as the center of the reactor then adds the dimensional components of each source to get their position in the cell's geometry. An array to store the calculated scalar fluxes is initialized, then a ray tracing method is performed to calculate distances and materials between the source point and experiment point.

Ray tracing is an appealing method to perform position optimization as both experiment and source locations are expressed at points within the geometry and the parameter to be whose difference needs to be minimized between experiment and calculation (scalar flux) can be easily calculated from the source activities with knowledge of the distances and materials between the source and end point. With each call of the material and distance function, the cell geometry is constructed from the material regions specifed in the geometry discretization as well as the water in the pool and void box installed on the west face of the reactor before each experiment. All source points are looped over all experiment positions provided to the function as input. Several lists are initialized to be added to or changed as the ray between source and end point is traced, including the storage list to be returned. The direction vector between the source and end point is calculated then the distance to the next material calculated. Interactions are determined by x position as the ray is traced. Each time a new material is encountered, the material and distance from the ray's previous point is recorded and the interaction point set as the updated point until reaching the destination point.

While many of the material transitions were relatively simple to specify, some either required a different check for interaction or a repeated interaction check due to the geometry of the material region. A function was written to calculate a line's intersection point with a specified plane to check for interaction of the ray with slanted portions of the window opening. By providing two points on the ray and a

point on the plane as well as a vector normal to the plane's surface, the intersection point (or indeed if there is an intersection) between the two is calculated. The dot product of the specified perpendicular vector of the plane and difference between the two points in the ray is taken. If this value is greater than a predefined minuscule tolerance, the line and plane intersect and the intersection point computed. If not, the line is considered parallel and None returned.

Another area difficult to determine interactions within is the lead experiment box at the center of the room as there are a large number of surfaces and high probability of reentry of a ray once it exits one of the box's faces. The box's geometry is constructed with rectangular blocks only increasing the number of possible interactions as even if a ray does not exit the lead box, it may exit a face of one of the construction boxes, requiring a point update and material check before extending the ray further. A while loop extends the ray through the box until exiting from one of the outer faces of the box. The rays are then traced to the final endpoints: the positions of the experiment foils, and the next ray traced until all source points have rays to all experiment points.

With the lists of distances and materials, scalar flux for each experiment point is calculated for the reactor optimization position. Cross sections and source activities are read into the optimization point object, and flux calculated for each ray traced to an experiment point with the flux from an isotropic source equation

$$\phi = \sum_{s=1}^{N_{\text{sources}}} \frac{A_{\text{s}}}{4\pi R_{\text{total}}} \prod_{m=1}^{N_{\text{materials in ray s}}} e^{-\Sigma_{a,m} R_m}. \tag{4.2}$$

After calculating these scalar fluxes for each experimental point, the difference between each calculated and total measured flux is taken, then the mean and variance of the set of differences determined. The calculated mean and variance are compared

to previous values and the smaller of the two stored along with the minimized optimization point for each point evaluated. The minimized mean and variance reactor positions are output to be used in angular discretization of the boundary condition.

4.4.2 Flux Weighting by Quadrature Angle

The reactor's position in relation to the cell is now determined, allowing discrete angles to be evaluated between source points and locations of fitted flux on the east wall. A Python script reads the fitted points from both energy groups and combines the data into one array with columns specifying position, epithermal flux, and thermal flux in order. The source nodes are read in and placed in the cell geometry using results from the spatial optimization script.

For each point on the wall with fitted flux, discrete angles and weights for the angles are calculated. Looping through all reactor source points for each wall point, the normalized direction vector between the two is determined, and approximation to flux at this point calculated using a simplified version of Equation 4.2 that only takes into account the water and void box between the source point and wall. All flux values calculated at this point are summed and each angle's flux is divided by the total to yield the weight. The discrete angles and weights are then stored for each wall point.

Wall points now have flux specified by wall position and angle, but only angles in the quadrature set specified may be used in the transport calculation. Several angular quadrature sets in PDT's libraries are copied into functions where the p-level and quadrature type can be specified for the quadrature to be used in the simulation and angles in quadrature returned. Sets with a large number of angles are desired for higher angular accuracy, so large p-level (14 to 24) level symmetric, linear discontinuous finite element, and Gauss-Legendre Chebishev angular quadrature sets

were explored as potential options and are available to discretize angle within.

To find the closest angles in quadrature for the discrete angles calculated for each point, the tensor dot product is taken between the two. The indices of the maximums in the resultant array are then found along the second dimension's axis which yields the index of the closest quadrature point for each angle at the wall point. The calculated angles are looped over and weights for each original discrete angle are added to a dictionary of the quadrature point indices for closest angles in a new entry if the found closest quadrature angle is not in the dictionary or added to the angle if the quadrature index is already present. After creating the weight dictionary for each wall point, an output file with wall point, angular quadrature (in terms of mu, eta, and xi), the total flux weight, and neutron flux by group is written to be used in PDT input. The weights are then written for each point and angle by line and entry respectively so the input generation script can separate the weights from the fluxes to reduce the number of sampled variables that need to be generated for uncertainty quantification.

4.5 PDT Input File Generation

The cell geometry, material properties, and boundary condition on the east wall need to be provided as input to PDT to run simulations. All information to specify these simulation parameters is found in output files from previous scripts. PDT uses XML (EXtensible Markup Language) to detail input and methods to be used in the simulation. While XML is easily machine and human readable, explicitly enumerating all parameters in XML nodes makes for verbose input. A Python script is developed to generate input files from calculated script outputs of parameters the simulation requires. After opening the file and writing the header, solution methods, method parameters, and aggregation factors used in parallelizing the run

are written based on internal variables which can be easily changed to suit the user's need and/or simulation's requirements. Energy group and angular quadrature nodes are then passed to the input.

Spatial input by dimension is contained in the first set of nodes using output from the geometry discretization script. The cell geometry csv file is opened and each dimension's divisions are defined by the number of cells as well as start and end points in the given dimension. With all three dimensions' divisions established, the cells form the three dimensional array that discretizes the cell's geometry. Data from cross section files are read in at runtime, but the names and locations of the files are specified in the input file. Density for each material must also be provided in the input depending upon the units of the cross sections. As the cross sections previously calculated from the Python script are given in units of barns (10^{-24} cm^2), material densities are specified in atoms/barn-cm. Component and material XML nodes are written then material distributed within the problem geometry. Material regions from the geometry discretization script are already defined by name, material, and start/end cell numbers for the cell discretization. Regions are looped over and written to the input file to assign all cells in the geometry a material.

The last set of simulation specifications make up the model's boundary condition. Depending upon the model's desired use, several different conditions are available to be written to the input file. A dummy boundary condition consisting of incident isotropic flux of consistent magnitude on the order of the average incident flux magnitude measured on the window for each group is distributed across the surface of the eastern irradiation cell's wall. The dummy boundary condition serves to benchmark simulation run time for the given resolution of the geometry. A boundary condition input developed specifically for this study allows flux at each wall location to be specified by angle and group. Angular determination output is read into an array

with flux by position and flux weight by point and angle. As the array is looped through each line, entries for all angles in the quadratre contributing to flux at the current point are written. Flux for each angle is written after multiplying the angle weight by total fitted flux at the point. The last boundary condition option available in the input generation script is for interaction with the uncertainty quantifcation script. Detailed further in Section 4.6, injection points are specified in the input template to write sampled variables to new input files. This boundary condition option uses the study specific boundary condition to break down flux by position and angle. Looping through the angular discretization output array by line, a check for writing epithermal and thermal flux is made by testing if either is specified as zero for the point's angle being written. If the group's flux needs to be written, an injection tag is created based upon the point number for the group and the angle number in the point to indicate which weight to apply to the sampled flux for the angle. Flux is sampled separately for each group; so the weights and distribution parameters output from angular discretization and flux fitting scripts respectively need to be broken up by group and reordered based upon their appearance in the input file. Files with the newly reordered distribution parameters and angular weights for each group are output for use in the uncertainty quantification script. After the boundary conditions are written, XML nodes remaining open are closed and the PDT input file is ready to be run.

4.6 Model Validation

To validate the computational results, model inputs are perturbed (specifically, the flux magnitudes of the boundary condition) with the goal of the perturbed results bounding the experimental data collected in the cell. In order to accomplish this task, a Python script is developed that samples variables from a given distribution,

disseminates the sampled variables in simulation input files, runs PDT for generated input files, and collects results from output. The developed system is dubbed "heron" and is written to be abstract and flexible enough to be extensible for other PDT users to utilize in their research.

Before a heron job is executed, a Python file with required inputs needs to be provided. Job parameters such as the working directory, template input file name, collected output file name, system specification, PDT executable path, and number of processors are are first defined, and optional variables may be provided such as job name, whether to echo the script's progress, and whether to run simulations (will just generate input files with sampled variables then terminate the job if false). Simulation details are then given including the type of mesh the problem is run on, total number of groups, and the numbers of the groups desired to be collected. The types of results to collect are also established as well as how to collect said results. The only option the script supports at present is collection by position, where a list of tuples needs to be furnished that correspond to points in the mesh that heron will match to cells to find their average flux. Variable sets are then defined by a list of tuples designating the variable set's name, the type of variable set, the distribution used, and number of samples to generate for this variable set. Current variable set types include named, file, and operand, where the distribution parameters are either spelled out in the current input file, provided by another file, or if the sampled variable needs to have an operation performed upon it before being inserted into the input file injection point, respectively. Any distribution in numpy's random method can be employed by naming it in the variable set definition provided the parameters are expressed in the form required by the given distribution. Number of samples must be expressed as an integer, and each variable set is sampled independently. Variable sets with the named type require the distribution parameters

to be expressed in the heron input file, while file and operand types require the user to indicate the locations of files with the parameters expressed in csv format. Operand types additionally require the specification of the type of operation and location of files with the matching operands listed. Associated PDT files with data such as cross sections, mesh, and angular quadrature must also be given in a list of strings for heron to copy into the simulation directory.

After creating the input file, the heron script is executed. A command line argument allows users to specify the heron input file without the need to manually add it to the python script. Input file variables are read and checks for optional variables performed to initialize them with default values if not originally enumerated. Lists of variables to be sampled are created by looping over the variable sets defined in input. Variable set names, distributions, and samples are added to the sample lists, while set distribution parameters are added to the sample list depending upon the set type. Named sets' list entries are pulled directly from the input file, file type sets generate an array from the specifed csv, and operand types work similarly to file types but generate lists of numbers from the provided operand file to perform operations upon sampled variables with in addition to generating list entries from designated files. A sample array is initialized and populated from a sample command using numpy's random package, constructed based on the input for each variable set, and expanded by performing the indicated operation if the variable set is operand type. The full sample input array is then assembled from the individual variable set sample arrays with each line being all sampled inputs for one simulation. Due to each variable set being sampled individually and all variable set samples interacting with each other, the total length of the array (and thus total number of simulations) is the product of the number of samples for all variable sets. The run directory is created and listed files associated with the PDT run are copied into the run directory.

At this point, simulations can be set up and results generated. A loop produces input files, runs the simulations and collects output. The input template is numbered and copied to the run directory. A dictionary is created between the injection tags and sampled variable value for that simulation, and then the inserted into the input file by reading the file contents, replacing the tags with the values in the dictionary, and writing the new file data back to the simulation input. Heron then issues a system command to run PDT based on the indicated system and number of processors. After the simulation is completed, output files are parsed to find cells that contain the points listed in the result collection variable in heron's input. As each cell is found and results collected, the line number, file number, and (if applicable) folder number are recorded so that in subsequent successful simulations the output files need not be sifted through to record results. Sampled variables for the simulation as well as results are written to the output csv file as they are collected for each simulation loop to ensure that what results are collected are communicated to the user in the event that allocated wall time for the heron run is not sufficient to run all simulations.

5. MODEL AND VALIDATION

Model results are presented in this chapter. Simulation solution methods and tolerances are given in an effort to provide transparent and reproducable results followed by visualization of model results in the cell for the two energy groups. Nominal model results are compared to experimental results as well as simplified models and an attempt to identify a spatial directionality of computational results is made. The perturbed results are presented with the goal of bounding experimental findings with a subsequent discussion of these results.

5.1 Simulation Parameters

As a maturing radiation transport code, myriad computational methods are available for use in PDT. Methods and tolerances utilized in model development are presented to allow reproducibility of results. Piecewise linear discontinuous (PWLD) method is used to solve the problem spatially with unlumped finite elements. To iterate over energy groups within group sets in the input, the generalized minimal residual method (GMRES) is employed. The GMRES method is set to restart if not converged within 12 iterations with a residual tolerance of 1.0e-8 and maximum number of iterations set at 1000. Pointwise tolerance for the energy group calculation solutions is 1.0e-7 with a maximum of 100 pointwise iterations. The angle set iterative method specified for the model is the Richardson method with 1.0e-7 residual tolerance and 1000 maximum residual iterations with a 1.0e-7 pointwise tolerance and 1000 pointwise iteration limit. Partitioning the problem is fairly simple due to the regular Cartesian geometry chosen and use of rigid angular quadrature sets. The spatial grid is 72 x 72 x 48 cells and quadrature set able to be solved in octants; so the problem is optimally partitioned with 512 processors into a 4 x cell by 8 y cell by

16 z cell configuration and aggregation factors of 1 x 9 x 3. Only one energy group set is specifed for the two groups with a thermal upper energy limit of 1 eV and epithermal upper limit of 60 eV. As detailed in Section 4.4.2, the angular quadrature employed is linear discontinuous finite element at its third level of resolution with 2048 angles. The boundary condition to generate the nominal model presented allows specification of incident flux by point and angle which requires tolerances to match within the constructed mesh and within angular quadrature. Tolerances for the geometry and angular matching are 1.0e-8 and 1.0e-6 respectively.

5.2 Model Results

Nominal model results are obtained, and PDT generates silo files to aid in visualizing the model results. VisIt is utilized to view these results. While the cell positions of validation data collection foils are given in bold in Appendix A, a visual aid to demonstrate these locations in the cell is presented in Figure 5.1. The labels in this figure correspond to foil location IDs of the validation points.

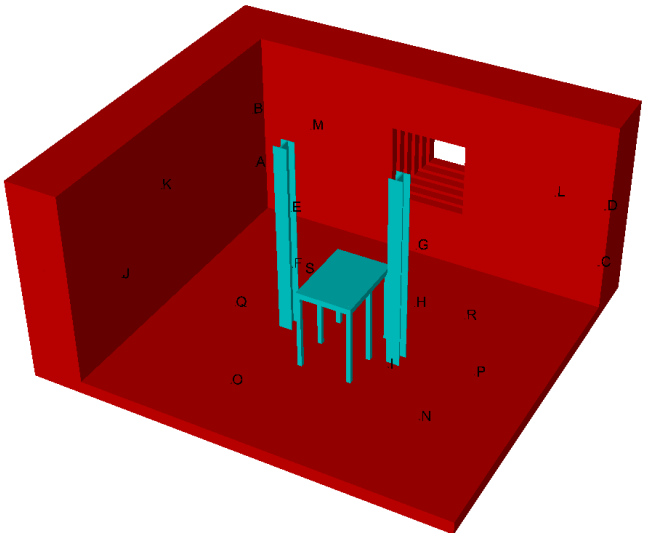

Figure 5.1: Locations of validation data collection in throughout the cell.

Figures 5.2 and 5.3 are generated using VisIt and demonstrate some interesting features in the results. The directionality imparted by the reactor being offset from the cell window is not obvious here but will be in the experiment comparisons. Interesting features of the flux model that are present in the visualizations are the shadows, or dips in flux, behind the steel structural beams, experiment table, and lead box. Both energy regions have small amounts of negative flux towards the outside edges of the concrete which may be mitigated by using the mass lumped version of PWLD. Ray effects are present, as evidenced by the hole towards the middle of the high magnitude beams and lumps toward the edges, though comparisons to experimental data will need to be made before concluding how badly they affect the model's predictive qualities.

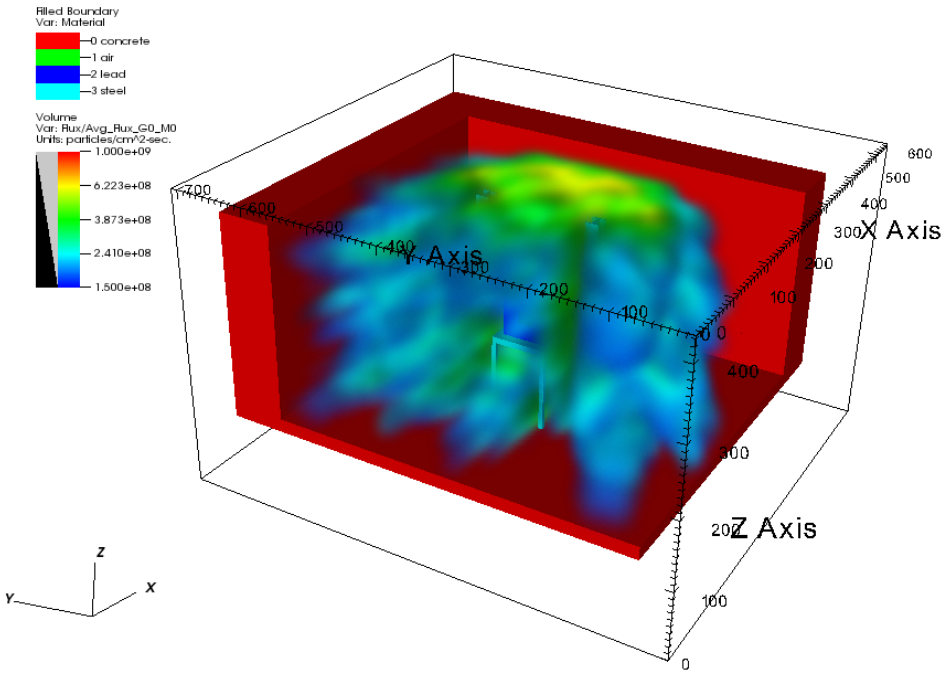

Figure 5.2: Visualization of cell volume average flux for epithermal energy range.

The epithermal region of the model is shown to be highly spatially and angularly dependent. The streaming quality of the neutrons is much more prominent in this energy region with less of a diffusive nature being present. This seems to make ray effects more conspicuous as flux can vary significantly with a relatively small change in volume. The flux beams end quite abruptly and ray effects give way to flux values not on the visible plotting color spectrum near mid to high flux areas. The epithermal region's fluxes are much lower in magnitude than the thermal group's though this is expected as epithermal flux on the boundary has lower magnitude and epithermal neutrons will contribute to the thermal group as they scatter within the cell.

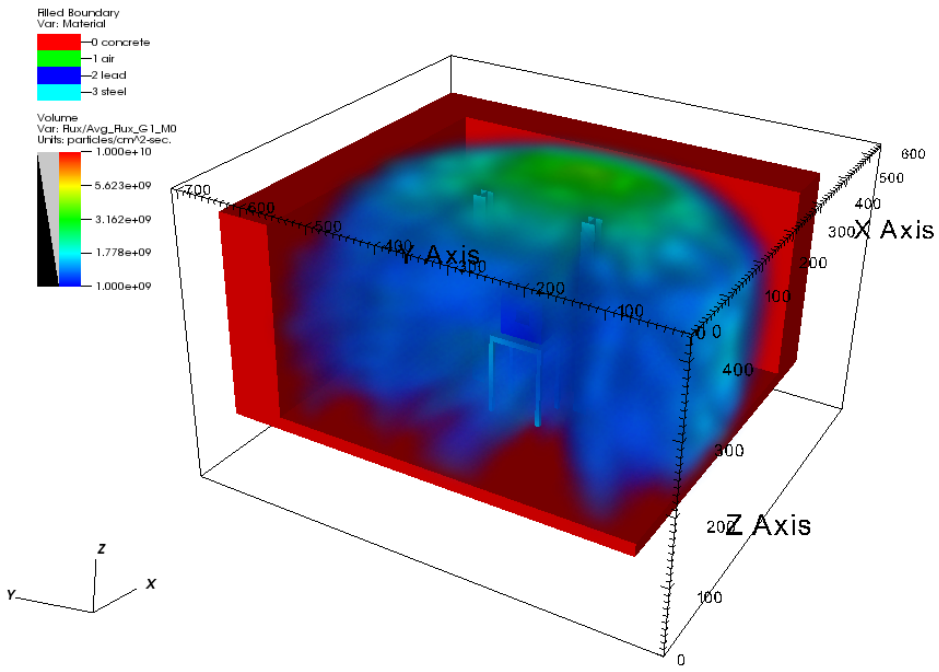

Figure 5.3: Visualization of cell volume average flux for thermal energy range.

The thermal group results are much more diffusive (especially closer to the window) and ray effects are not as prominent. Flux values still vary in angle, but do not

seem to suffer from as great of differences as the epithermal region. The magnitude of the thermal region is much higher than the epithermal throughout the cell as well due to the lack of losses, higher flux on the boundary, and epithermal neutron scatters contributing to the thermal flux.

While the visualizations give general qualitative impressions of the model, it will be more informative to perform a qualitative comparison of cell flux results to experiment data. Figures 5.4 and 5.5 plot experiment and model flux values at the same cell positions while the data for these plots can be found in Tables 5.1 and 5.2.

Epithermal results (Fig. 5.4 and Table 5.1) appear to be overestimated the closer and more within view of the window the collection point is and severely underestimated the further out of the window's view collection points are. Points E through H are collected from the support beams facing towards the window and are greatly overestimated; whereas points A through D are collected on the north (points A and B) and south (points C and D) walls only about a foot away from the east wall

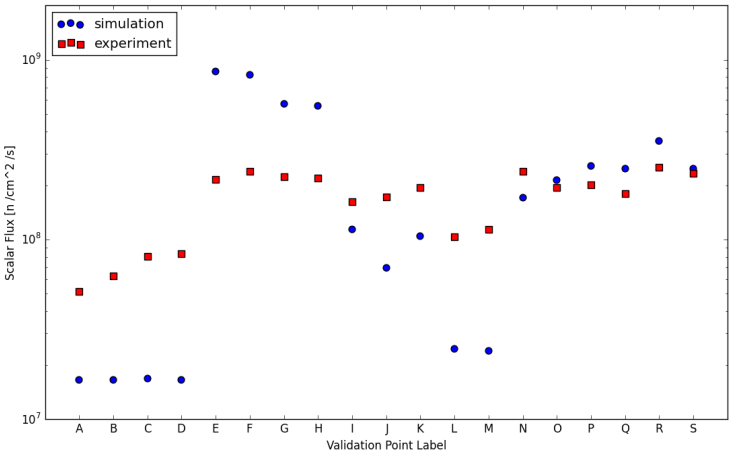

Figure 5.4: Comparison of nominal model and experiment epithermal flux at various cell locations.

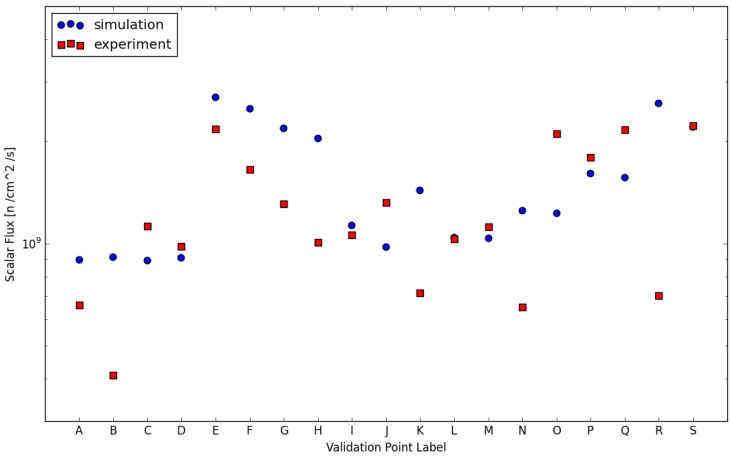

Figure 5.5: Comparison of nominal model and experiment thermal flux at various cell locations.

separating the pool from the cell with model results underestimating the experiment. Further evidence for this spatial edge underestimation can be found in points L and M. Results further away from the incident neutron boundary appear to have much less variance in results (points I, N-S).

Thermal results (Fig. 5.5 and Table 5.2) look much more promising than the epithermal, but the the largest differences between experiment and computational model results are still closer to the window. There appears to be some spatial bias present in the experiments conducted that the computational model has not accounted for (or could be outlying data) as the north wall collection points (points A and B) are over estimated and south wall points (C and D) are slightly overestimated by the nominal model. Results seem to capture the general behavior for points E through H though are overestimated. Several points (I, M, P, S) are very accurately predicted.

Table 5.1: Epithermal Experiment Data and Nominal Model Results

Validation Pos. ID	Epithermal Scalar Flux [n cm^{-2} s^{-1}]	
	Experiment	Nominal Comp.
A	5.1242e+07	1.6580e+07
B	6.2608e+07	1.6557e+07
C	8.0885e+07	1.6851e+07
D	8.3702e+07	1.6633e+07
E	2.1637e+08	8.5683e+08
F	2.3925e+08	8.2701e+08
G	2.2259e+08	5.6947e+08
H	2.1900e+08	5.5567e+08
I	1.6239e+08	1.1383e+08
J	1.7307e+08	6.9482e+07
K	1.9514e+08	1.0459e+08
L	1.0328e+08	2.4694e+07
M	1.1410e+08	2.3960e+07
N	2.3979e+08	1.7014e+08
O	1.9470e+08	2.1311e+08
P	2.0152e+08	2.5751e+08
Q	1.8068e+08	2.4820e+08
R	2.5158e+08	3.5402e+08
S	2.3297e+08	2.4758e+08

Table 5.2: Thermal Experiment Data and Nominal Model Results

Validation Pos. ID	Thermal Scalar Flux [n cm^{-2} s^{-1}]	
	Experiment	Nominal Comp.
A	6.5816e+08	8.9599e+08
B	4.0887e+08	9.1307e+08
C	1.1263e+09	8.9241e+08
D	9.8333e+08	9.0853e+08
E	2.1798e+09	2.6961e+09
F	1.6573e+09	2.4924e+09
G	1.3071e+09	2.1849e+09
H	1.0072e+09	2.0448e+09
I	1.0598e+09	1.1290e+09
J	1.3203e+09	9.7723e+08
K	7.1715e+08	1.4357e+09
L	1.0337e+09	1.0409e+09
M	1.1199e+09	1.0360e+09
N	6.4910e+08	1.2527e+09
O	2.1073e+09	1.2270e+09
P	1.7991e+09	1.6083e+09
Q	2.1662e+09	1.5637e+09
R	7.0266e+08	2.5872e+09
S	2.2265e+09	2.2081e+09

5.3 Boundary Condition Comparisons

In order to determine whether some aspects of model development are necessary to accurately characterize flux in the cell, models with simpler construction are run and compared to the fully developed model's results and experiments. The two less developed models ignore flux magnitude spatial changes on the boundary or use an isotropic angular distribution on the boundary respectively. The first uses an isotropic boundary source with the mean values of the window fits for flux magnitudes in each group across the entire wall, and the other uses the fitted flux values on the window but with angular weights equally distributed for all angles incident upon the irradiation cell's boundary.

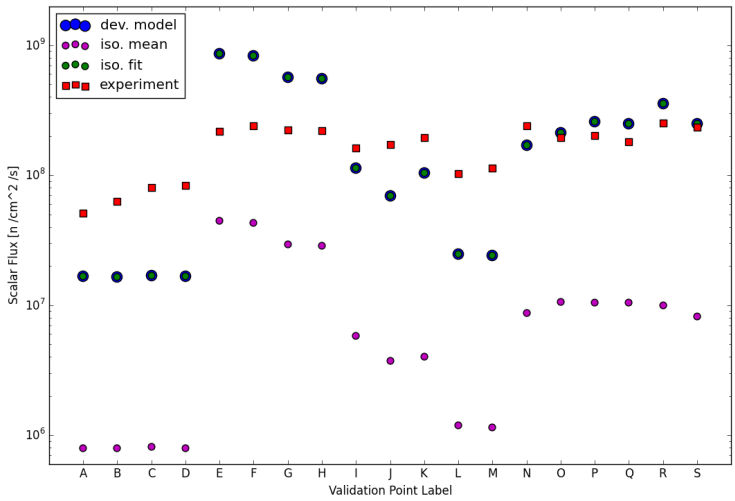

Figure 5.6: Comparison of developed and simpler models and experiment epithermal flux at various cell locations.

In the epithermal region, the isotropic mean model severely underestimates experiment data for all points. The isotropic window fit yields results disturbingly

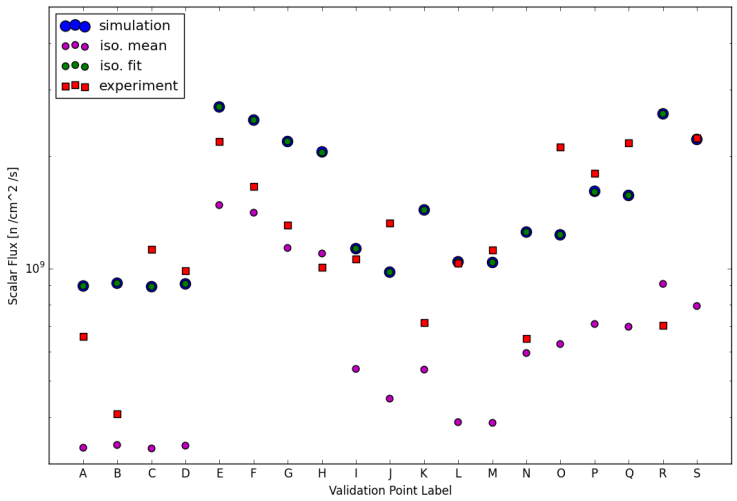

Figure 5.7: Comparison of developed and simpler models and experiment epithermal flux at various cell locations.

similar to the developed model. The implication that an isotropic distribution of fitted flux magnitude will work just as well as the angular distribution developed would suggest a low dependence of flux spatial distribution on incident angle of neutrons into the cell, but it is more likely that the intermediate boundary condition source is dominating the solution of these two models, making angular dependence of a lower strength source irrelevant. The isotropic model also requires specification of flux for all incident angles on the edge which increased the runtime of the simulation to around 23 minutes compared to the 7 minutes that the fully developed model requires to complete its run. These models' trends continue in the thermal region, though the mean isotropic boundary condition predicts some points (F, G, H, K, N, and R) more accurately than the fully developed model.

5.4 Validation Parameters

Input to the validation framework script requires the job parameters and variable sets to be defined. In the interest of reproducibility, the heron script input is detailed for the validation simulations. Run on 32 nodes on Lawrence Livermore National Laboratory's cab machine with 512 processors, PDT simulations used a locally compiled version of PDT. The 3D block mesh type is specified for the collecting results for both energy groups. Results collected are the average flux in cells containing points at which validation data is measured. Two variable sets are used, one for each group in energy. Both variable sets are of the operand type with normal distributions and are sampled 9 times individually (making 81 total simulations). The variable distributions and weights to multiply sampled fluxes for both energy groups has been generated already by the PDT input generation script. Associated PDT files to be copied to the run directory include the cross section files and angular quadrature file.

5.5 Validation Results

By perturbing the flux incident upon the cell, points where the experimental data is within realistic computational result bounds are identified. These bounded points establish where the model is predicting experimental results with a certain degree of confidence. The epithermal validation results (Fig. 5.8 and Table 5.3) show that there are some serious problems with the model in this energy group. Only points O and S fall within the computed validation bounds and both are towards the edges of the data. The thermal validation results (Fig. 5.9 and Table 5.4) are more promising. Nine out of the nineteen data points fall within validation bounds with behaviors captured, but overestimated for points E through H, K, N, and R and an unaccounted bias in two outliers (points A and B).

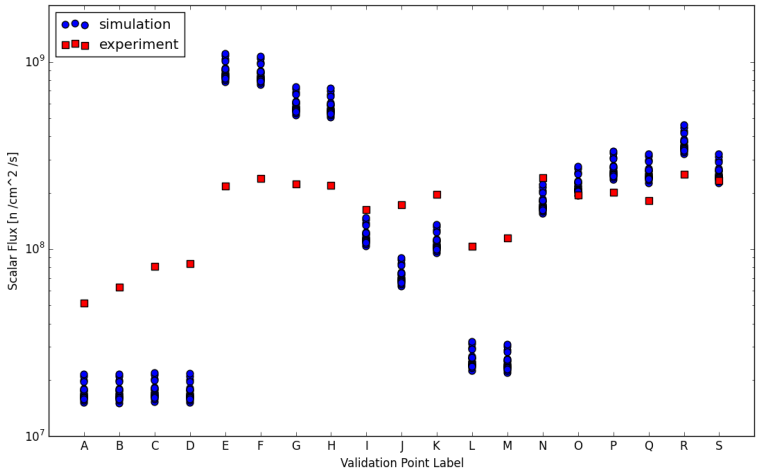

Figure 5.8: Epithermal experiment and perturbed computational model results at data collection points.

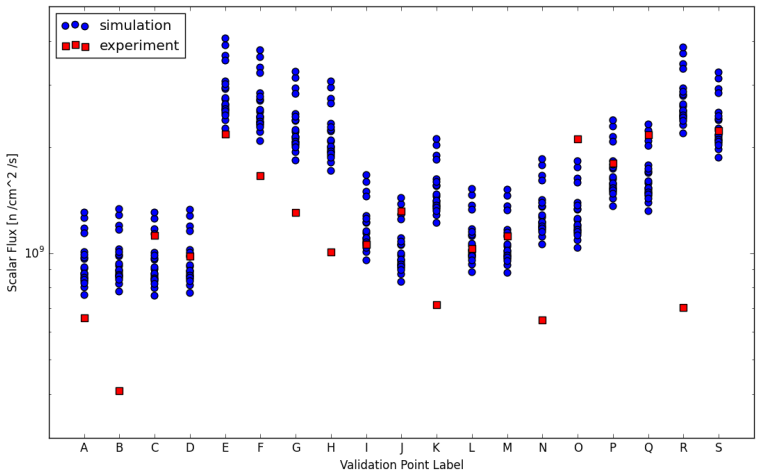

Figure 5.9: Thermal experiment and perturbed computational model results at data collection points.

Table 5.3: Epithermal Experiment Data and Validation Bound Results

Validation Pos. ID	Epithermal Scalar Flux [n cm^{-2} s^{-1}]		
	Experiment	Low Comp.	High Comp.
A	5.1242e+07	1.5027e+07	2.1431e+07
B	6.2608e+07	1.5007e+07	2.1402e+07
C	8.0885e+07	1.5273e+07	2.1780e+07
D	8.3702e+07	1.5075e+07	2.1499e+07
E	2.1637e+08	7.7657e+08	1.1075e+09
F	2.3925e+08	7.4954e+08	1.0690e+09
G	2.2259e+08	5.1615e+08	7.3600e+08
H	2.1900e+08	5.0363e+08	7.1825e+08
I	1.6239e+08	1.0317e+08	1.4713e+08
J	1.7307e+08	6.2973e+07	8.9812e+07
K	1.9514e+08	9.4789e+07	1.3519e+08
L	1.0328e+08	2.2381e+07	3.1918e+07
M	1.1410e+08	2.1716e+07	3.0970e+07
N	2.3979e+08	1.5422e+08	2.1986e+08
O	1.9470e+08	1.9315e+08	2.7546e+08
P	2.0152e+08	2.3342e+08	3.3275e+08
Q	1.8068e+08	2.2495e+08	3.2082e+08
R	2.5158e+08	3.2086e+08	4.5760e+08
S	2.3297e+08	2.2439e+08	3.2002e+08

Table 5.4: Thermal Experiment Data and Validation Bound Results

Validation Pos. ID	Thermal Scalar Flux [n cm^{-2} s^{-1}]		
	Experiment	Low Comp.	High Comp.
A	6.5816e+08	7.6376e+08	1.3090e+09
B	4.0887e+08	7.7834e+08	1.3339e+09
C	1.1263e+09	7.6074e+08	1.3037e+09
D	9.8333e+08	7.7451e+08	1.3272e+09
E	2.1798e+09	2.2578e+09	4.0653e+09
F	1.6573e+09	2.0860e+09	3.7618e+09
G	1.3071e+09	1.8349e+09	3.2784e+09
H	1.0072e+09	1.7158e+09	3.0726e+09
I	1.0598e+09	9.5756e+08	1.6645e+09
J	1.3203e+09	8.3046e+08	1.4357e+09
K	7.1715e+08	1.2193e+09	2.1116e+09
L	1.0337e+09	8.8706e+08	1.5214e+09
M	1.1199e+09	8.8286e+08	1.5143e+09
N	6.4910e+08	1.0605e+09	1.8532e+09
O	2.1073e+09	1.0356e+09	1.8247e+09
P	1.7991e+09	1.3595e+09	2.3857e+09
Q	2.1662e+09	1.3207e+09	2.3227e+09
R	7.0266e+08	2.1875e+09	3.8355e+09
S	2.2265e+09	1.8702e+09	3.2638e+09

6. CONCLUSIONS AND FUTURE WORK

The work performed spans the areas of experimentation, data collection, modeling, and validation. While the predictive capabilities of the current model are questionable, general behavior in terms of flux prediction with respect to collection points' cell position give indications of the model's spatial strengths and weaknesses. Points close to and within view of the irradiation window are typically overestimated in both energy groups, while those outside the cell window's view are severely underestimated in the epithermal range likely due to only low energy neutron flux being collected from experiments. In reality, the epithermal group neutrons will have sources throughout the cell in the form of higher energy groups' contribution as neutrons from higher energies scatter down into lower energy groups. To account for the higher energy neutrons, experiments with a greater range in energy detection bounds is necessary. Until the higher energy groups can be incorporated into the model, it is unlikely that the epithermal model will be able to depict the epithermal neutron behavior very accurately. The thermal flux predictions tend to be both more accurate (with nine of the experiment points agreeing with the model) and better able to predict behaviors of the experiments. In the case of points E through H, the thermal model demonstrates the negative trend evidenced in experiment data. While less than half of the experiment data agrees with the model, by collecting data through additional experiments and better calibration of boundary condition input, this first step may yield results that can be used to predict sample dose in this energy region at least.

While efforts have yielded a framework to characterize neutron flux throughout the irradiation cell, the model's predictive capability could undergo further re-

finement with the inclusion of additional considerations. To properly account for measurement error of foils from the high purity germanium activity counts, the error would need to be propagated through all points where measured flux informs the computational model as well. Starting with flux fitting, the measurement error needs to be considered along with the standard fitting error when sampling fluxes for validation. Also to be considered is the fact that the reactor's position changes slightly for every experiment. Not only will this affect the flux magnitude, but the angular distribution of flux. To account for these minute positional changes, the angular distribution of flux on the cell's boundary would need to be perturbed. The most likely way to do this would be to establish some sort of error bounds for the angular weights. The change in reactor position will also likely add more angles contributing to the flux at fitted points on the cell's east wall; so the reactor position optimization script would need to be utilized extensively to explore which angles are possible for probable reactor locations. An obvious way to increase model accuracy is to provide better input by running more experiments to better inform model inputs. A final further consideration is that current results only use P0 scattering cross sections. A more mature study would increase the scattering level to more realistically represent downscattering from the epithermal to thermal energy regions.

REFERENCES

[1] *Standard Specification for Cold-Formed Welded and Seamless Carbon Steel Structural Tubing in Rounds and Shapes.* American National Standard, USA, 1978.

[2] *Nuclear Science Center Safety Analysis Report.* Texas Engineering Experiment Station, College Station, Texas, 2011.

[3] *Nuclear Science Center Standard Operating Procedures.* Texas Engineering Experiment Station, College Station, Texas, 2015.

[4] *Livermore Computing Center.* Lawrence Livermore National Laboratory, 2016. Retrieved from https://computing.llnl.gov/

[5] Parasol Algorithms and Applications Group. Generic particle transport code, 2012.

[6] D. Ascher, P.F. Dubois, K. Hinsen, J. Hugunin, and T. Oliphant. *Numerical Python.* Lawrence Livermore National Laboratory, Livermore, California, USA, 2015.

[7] Edward M. Baum, Knox Harold D., and Thomas R. Miller. *Nuclides and Isotopes.* Lockheed Martin Distribution Services, Cherry Hill, NJ, 2002.

[8] George I. Bell and Samuel Glasstone. *Nuclear Reactor Theory.* Robert E. Krieger Publishing Company, Malabar, FL, 1970.

[9] Hank Childs, Eric Brugger, Brad Whitlock, Jeremy Meredith, Sean Ahern, David Pugmire, Kathleen Biagas, Mark Miller, Cyrus Harrison, Gunther H. Weber, Hari Krishnan, Thomas Fogal, Allen Sanderson, Christoph Garth, E. Wes Bethel, David Camp, Oliver Rübel, Marc Durant, Jean M. Favre, and Paul Navrátil. VisIt: An End-User Tool For Visualizing and Analyzing Very Large

Data. In *High Performance Visualization–Enabling Extreme-Scale Scientific Insight*, pages 357–372. Oct 2012.

[10] United States Regulatory Commission. 10 CFR 20.1201 Subpart C Occupational Dose Limits, 2010.

[11] Christian Grossmann, Hans-Gorg Roos, and Martin Stynes. *Numerical Treatment of Partial Differential Equations*. Springer Berlin Heidelberg, New York, NY, 2007.

[12] K.D. Lathrop. Ray effects in discrete ordinates equations. 1968.

[13] Lenntech. Chemical elements listed by density, 2016.

[14] E.E. Lewis and W.F. Miller Jr. *Computational Methods of Neutron Transport*. American Nuclear Society, La Grange Park, IL, 1993.

[15] T.E. Northup. *High-Density Concrete for Gamma and Neutron Attenuation*. Oak Ridge National Laboratory, Oak Ridge, TN, 1965.

[16] DOE Office of Nuclear Energy. Predictive simulation. 2014.

[17] Organisation for Economic Co-operation and Development, Paris, France. *JANIS 4.0 User's Guide*, 2013.

[18] R Core Team. *R: A Language and Environment for Statistical Computing*. R Foundation for Statistical Computing, Vienna, Austria, 2016.

[19] James E. Turner. *Atoms, Radiation, and Radiaion Protection*. Wiley-VCH, Germany, 2007.

[20] G. van Rossum and F.L. Drake (eds). *Python Reference Manual*. PythonLabs, Virginia, USA, 2016.

APPENDIX A

FLUX FOIL EXPERIMENT POSITIONS

Experiment No.	Foil No.	Location ID	Foil Cell Position [cm]		
			x	y	z
1	1	1-1	567.69	304.165	118.11
1	2	1-2	567.69	304.165	135.89
1	3	1-3	567.69	304.165	156.21
1	4	1-4	567.69	304.165	173.99
1	5	1-5	567.69	276.225	118.11
1	6	1-6	567.69	276.225	135.89
1	7	1-7	567.69	276.225	156.21
1	8	1-8	567.69	276.225	173.99
1	9	1-9	567.69	248.285	118.11
1	10	1-10	567.69	248.285	135.89
1	11	1-11	567.69	248.285	156.21
1	12	1-12	567.69	248.285	173.99
2	1	2-1	567.69	297.815	123.19
2	2	2-2	567.69	297.815	138.43
2	3	2-3	567.69	297.815	153.67
2	4	2-4	567.69	297.815	168.91
2	5	2-5	567.69	282.575	123.19
2	6	2-6	567.69	285.115	146.05
2	7	2-7	567.69	264.795	146.05

Experiment No.	Foil No.	Location ID	Foil Cell Position [cm]		
			x	y	z
2	8	2-8	567.69	282.575	168.91
2	9	2-9	567.69	267.335	123.19
2	10	2-10	567.69	274.955	135.89
2	11	2-11	567.69	274.955	156.21
2	12	2-12	567.69	267.335	168.91
2	13	2-13	567.69	252.095	123.19
2	14	2-14	567.69	252.095	138.43
2	15	2-15	567.69	252.095	153.67
2	16	2-16	567.69	252.095	168.91
4	1	4-1	567.69	292.735	171.45
4	2	4-2	567.69	287.655	166.37
4	3	4-3	567.69	262.255	166.37
4	4	4-4	567.69	257.175	171.45
4	5	4-5	567.69	277.495	148.59
4	6	4-6	567.69	282.575	158.75
4	7	4-7	567.69	267.335	158.75
4	8	4-8	567.69	272.415	148.59
4	9	4-9	567.69	277.495	143.51
4	10	4-10	567.69	282.575	133.35
4	11	4-11	567.69	267.335	133.35
4	12	4-12	567.69	272.415	143.51
4	13	4-13	567.69	292.735	120.65
4	14	4-14	567.69	287.655	125.73

Experiment No.	Foil No.	Location ID	Foil Cell Position [cm]		
			x	y	z
4	15	4-15	567.69	262.255	125.73
4	16	4-16	567.69	257.175	120.65
5	1	5-1	567.69	292.735	163.83
5	2	5-2	567.69	282.575	158.75
5	3	5-3	567.69	267.335	158.75
5	4	5-4	567.69	257.175	163.83
5	5	5-5	567.69	292.735	151.13
5	6	5-6	567.69	285.115	146.05
5	7	5-7	567.69	264.795	146.05
5	8	5-8	567.69	257.175	151.13
5	9	5-9	567.69	292.735	140.97
5	10	5-10	567.69	274.955	156.21
5	11	5-11	567.69	274.955	135.89
5	12	5-12	567.69	257.175	140.97
5	13	5-13	567.69	292.735	128.27
5	14	5-14	567.69	282.575	133.35
5	15	5-15	567.69	267.335	133.35
5	16	5-16	567.69	257.175	128.27
6	1	6-1	567.69	274.955	161.29
6	2	6-2	567.69	274.955	130.81
6	3	6-3	567.69	290.195	146.05
6	4	6-4	567.69	259.715	146.05
6	5	6-5	567.69	268.605	152.4

Experiment No.	Foil No.	Location ID	Foil Cell Position [cm]		
			x	y	z
6	6	6-6	567.69	277.495	148.59
6	7	6-7	567.69	272.415	148.59
6	8	6-8	567.69	277.495	143.51
6	9	6-9	567.69	272.415	143.51
6	10	6-10	567.69	268.605	139.7
6	11	6-11	567.69	281.305	152.4
6	12	6-12	567.69	281.305	139.7
6	13	6-13	567.69	285.115	135.89
6	14	6-14	567.69	285.115	156.21
6	15	6-15	567.69	264.795	156.21
6	16	6-16	567.69	264.795	135.89
7	1	7-1	567.69	304.165	168.91
7	2	7-2	567.69	304.165	153.67
7	3	7-3	567.69	304.165	138.43
7	4	7-4	567.69	304.165	123.19
7	5	7-5	567.69	247.015	168.91
7	6	7-6	567.69	247.015	153.67
7	7	7-7	567.69	247.015	138.43
7	8	7-8	567.69	247.015	123.19
7	**9**	**A**	**452.12**	**548.64**	**91.44**
7	**10**	**B**	**452.12**	**548.64**	**182.88**
7	**11**	**C**	**452.12**	**0**	**91.44**
7	**12**	**D**	**452.12**	**0**	**182.88**

Experiment No.	Foil No.	Location ID	Foil Cell Position [cm]		
			x	y	z
7	**13**	**E**	**251.46**	**365.91875**	**182.88**
7	**14**	**F**	**251.46**	**365.91875**	**91.44**
7	**15**	**G**	**251.46**	**180.49875**	**182.88**
7	**16**	**H**	**251.46**	**180.49875**	**91.44**
8	1	8-1	567.69	290.195	161.29
8	2	8-2	567.69	259.715	161.29
8	3	8-3	567.69	290.195	130.81
8	4	8-4	567.69	259.715	130.81
8	**5**	**I**	**0**	**91.44**	**203.2**
8	**6**	**J**	**0**	**457.2**	**203.2**
8	**8**	**K**	**215.9**	**548.64**	**182.88**
8	**9**	**L**	**482.6**	**81.28**	**162.56**
8	**10**	**M**	**482.6**	**467.36**	**162.56**
8	**11**	**N**	**147.32**	**119.38**	**0**
8	**12**	**O**	**93.98**	**370.84**	**0**
8	**13**	**P**	**261.62**	**93.98**	**0**
8	**14**	**Q**	**241.3**	**457.2**	**0**
8	**15**	**R**	**368.3**	**157.48**	**0**
8	**16**	**S**	**358.14**	**411.48**	**0**

APPENDIX B

FLUX FOIL EXPERIMENT RESULTS

Location ID	Scalar Flux [n cm^{-2} s^{-1}]	
	Thermal	Epithermal
1-1	6.1803E+10	5.5211E+09
1-2	1.7358E+11	1.1856E+10
1-3	2.2369E+11	1.4173E+10
1-4	1.5656E+11	9.6922E+09
1-5	2.5387E+11	1.3387E+10
1-6	5.5914E+11	3.3834E+10
1-7	7.6787E+11	4.4048E+10
1-8	4.1713E+11	2.8811E+10
1-9	1.1803E+11	7.2352E+09
1-10	3.0526E+11	1.9333E+10
1-11	5.0916E+11	2.6539E+10
1-12	3.1591E+11	1.9623E+10
2-1	1.8016E+11	8.5480E+09
2-2	3.3103E+11	1.7536E+10
2-3	3.6405E+11	2.0317E+10
2-4	2.4732E+11	1.4810E+10
2-5	3.0675E+11	1.7097E+10
2-6	6.7569E+11	3.1732E+10
2-7	6.5309E+11	4.1863E+10

Location ID	Scalar Flux [n cm^{-2} s^{-1}]	
	Thermal	Epithermal
2-8	5.1782E+11	2.8413E+10
2-9	3.7376E+11	1.7408E+10
2-10	6.2636E+11	2.8506E+10
2-11	7.0680E+11	4.1540E+10
2-12	5.9835E+11	3.6707E+10
2-13	2.5684E+11	1.2781E+10
2-14	3.7281E+11	2.4373E+10
2-15	4.5217E+11	3.5131E+10
2-16	4.2073E+11	2.2846E+10
4-1	3.1407E+11	1.5820E+10
4-2	4.1374E+11	2.3898E+10
4-3	5.3152E+11	3.5278E+10
4-4	3.6180E+11	2.5719E+10
4-5	5.5628E+11	3.6345E+10
4-6	5.0374E+11	3.2401E+10
4-7	5.7715E+11	3.9608E+10
4-8	6.5126E+11	3.7040E+10
4-9	5.9268E+11	3.1776E+10
4-10	4.6331E+11	2.2217E+10
4-11	4.4540E+11	2.6955E+10
4-12	6.1988E+11	3.5434E+10
4-13	1.9505E+11	9.0230E+09
4-14	2.5210E+11	1.4001E+10

Location ID	Scalar Flux [n cm^{-2} s^{-1}]	
	Thermal	Epithermal
4-15	3.1892E+11	1.9452E+10
4-16	2.0451E+11	1.1823E+10
5-1	3.5426E+11	1.9717E+10
5-2	4.9734E+11	3.0691E+10
5-3	6.6753E+11	4.3424E+10
5-4	5.0047E+11	3.6755E+10
5-5	4.4154E+11	2.3125E+10
5-6	5.2422E+11	3.0247E+10
5-7	7.4348E+11	4.2581E+10
5-8	5.3744E+11	4.0216E+10
5-9	4.1209E+11	2.2188E+10
5-10	6.5000E+11	3.7633E+10
5-11	6.5449E+11	2.7753E+10
5-12	5.2560E+11	3.6590E+10
5-13	2.6453E+11	1.2526E+10
5-14	4.3783E+11	2.4574E+10
5-15	4.8083E+11	2.9759E+10
5-16	3.2998E+11	1.9823E+10
6-1	7.1669E+11	3.6800E+10
6-2	5.1173E+11	2.7989E+10
6-3	4.9258E+11	2.9161E+10
6-4	6.0917E+11	4.2866E+10
6-5	6.4564E+11	4.7639E+10

Location ID	Scalar Flux [n cm^{-2} s^{-1}]	
	Thermal	Epithermal
6-6	6.0462E+11	4.2345E+10
6-7	6.4593E+11	4.2531E+10
6-8	6.5603E+11	3.7423E+10
6-9	6.9483E+11	3.8874E+10
6-10	6.9570E+11	3.6739E+10
6-11	5.9015E+11	3.5709E+10
6-12	5.7009E+11	3.2860E+10
6-13	5.4677E+11	2.6368E+10
6-14	5.0337E+11	2.9972E+10
6-15	6.4433E+11	4.9790E+10
6-16	5.8049E+11	3.3513E+10
7-1	6.2782E+10	5.2899E+09
7-2	8.0930E+10	5.9321E+09
7-3	7.9074E+10	6.3764E+09
7-4	4.3140E+10	3.3525E+09
7-5	1.4427E+11	1.2044E+10
7-6	1.8441E+11	1.4683E+10
7-7	1.8141E+11	1.1790E+10
7-8	9.0149E+10	5.6091E+09
A	**6.5816E+08**	**5.1242E+07**
B	**4.0887E+08**	**6.2608E+07**
C	**1.1263E+09**	**8.0885E+07**
D	**9.8333E+08**	**8.3702E+07**

Location ID	Scalar Flux [n cm^{-2} s^{-1}]	
	Thermal	Epithermal
E	**2.1798E+09**	**2.1637E+08**
F	**1.6573E+09**	**2.3925E+08**
G	**1.3071E+09**	**2.2259E+08**
H	**1.0072E+09**	**2.1900E+08**
8-1	4.2543E+11	2.5988E+10
8-2	5.6375E+11	4.5618E+10
8-3	1.6025E+11	9.4551E+09
8-4	1.3923E+11	1.2834E+10
I	**1.0598E+09**	**1.6239E+08**
J	**1.3203E+09**	**1.7307E+08**
K	**7.1715E+08**	**1.9514E+08**
L	**1.0337E+09**	**1.0328E+08**
M	**1.1199E+09**	**1.1410E+08**
N	**6.4910E+08**	**2.3979E+08**
O	**2.1073E+09**	**1.9470E+08**
P	**1.7991E+09**	**2.0152E+08**
Q	**2.1662E+09**	**1.8068E+08**
R	**7.0266E+08**	**2.5158E+08**
S	**2.2265E+09**	**2.3297E+08**

APPENDIX C

MATERIAL DENSITIES AND CHEMICAL COMPOSITIONS

Material	Density [g/cc]	Chemical Composition	
		Element	at% Composition
High density concrete [15]	2.4	H	48.4238
		O	32.0243
		Fe	16.0573
		Si	1.1876
		Al	0.1607
		Ca	1.9932
		Mg	0.1098
		S	0.0364
		Ti	0.0070
ASTM A500 Steel [1]	8.05	Fe	98.0370
		C	0.2700
		Mn	1.4000
		P	0.0500
		S	0.0630
		Cu	0.1800

Material	Density [g/cc]	Chemical Composition	
		Element	at% Composition
Air [13]	0.001225	N	78.0955
		O	20.9590
		Ar	0.9455
Lead Brick [13]	11.34	Pb	100